Beyond benchmarking: an expert-guided consensus approach to spatially aware clustering

Jieran Sun[1†], Kirti Biharie[2,3†], Peiying Cai[4†], Niklas Müller-Bötticher[5†], Paul Kiessling[6†], Meghan A. Turner[7†], Søren H. Dam[8,9†], Florian Heyl[10,11†], Sarusan Kathirchelvan[4], Martin Emons[4], Samuel Gunz[4], Sven Twardziok[5], Amin El-Heliebi[12], Martin Zacharias[13], SpaceHack 2.0 participants, Roland Eils[5], Marcel Reinders[3], Raphael Gottardo[1], Christoph Kuppe[6], Brian Long[7*], Ahmed Mahfouz[2,3*], Mark D. Robinson[4*], Naveed Ishaque[5*]

[1]Biomedical Data Science Center, Centre Hospitalier Universitaire Vaudois, Rue du Bugnon 21, 1011 Lausanne, Switzerland.
[2]Department of Human Genetics, Leiden University Medical Center, Einthovenweg 20, 2333 ZC Leiden, Netherlands.
[3]Delft Bioinformatics Lab, Delft University of Technology, Van Mourik Broekmanweg 6, 2628 XE Delft, Netherlands.
[4]Department of Molecular Life Sciences and SIB Swiss Institute of Bioinformatics, University of Zurich, Winterthurerstrasse 190, 8057 Zurich, Switzerland.
[5]Berlin Institute of Health at Charité – Universitätsmedizin Berlin, Center of Digital Health, Charitéplatz 1, 10117 Berlin, Germany.
[6]Department of Nephrology, Rheumatology, and Clinical Immunology, University Hospital RWTH Aachen, Pauwelsstraße 30, Aachen, Germany.
[7]Allen Institute for Brain Science, 615 Westlake Ave N, Seattle, WA, USA 98109.
[8]DTU Health Tech, Technical University of Denmark, Ørsteds Plads, Building 345C, 2800, Kgs. Lyngby, Denmark.
[9]LEO Foundation Skin Immunology Research Center, Department of Immunology and Microbiology, University of Copenhagen, Blegdamsvej 3B, 2200, Copenhagen N, Denmark.
[10]German Cancer Research Center (DKFZ), Division of Computational Genomics and Systems Genetics, Im Neuenheimer Feld 280, 69120 Heidelberg, Germany.
[11]The German Human Genome-Phenome Archive (GHGA), Im Neuenheimer Feld 280, 69120 Heidelberg, Germany.
[12]Division of Cell Biology, Histology and Embryology, Gottfried Schatz Research Center, Medical University of Graz, Graz, Austria.
[13]Diagnostic and Research Institute of Pathology, Medical University of Graz, Graz, Austria.

*Corresponding author(s). E-mail(s): brianl@alleninstitute.org; a.mahfouz@lumc.nl; mark.robinson@mls.uzh.ch; naveed.ishaque@bih-charite.de;
†These authors contributed equally to this work.

Abstract

Spatial omics technologies have revolutionized the study of tissue architecture and cellular heterogeneity by integrating molecular profiles with spatial localization. In spatially resolved transcriptomics, delineating higher-order anatomical structures is critical for understanding how cellular organization affects tissue and organ function. Since 2020, more than 50 spatially aware clustering (SAC) methods have been developed for this purpose. However, the reliability of current benchmarks is undermined by their narrow focus on Visium and brain tissue datasets, as well as incorrect interpretation of manual annotation as ground truth. Here, we present SACCELERATOR, a community-driven, extensible framework that standardizes data formatting, method integration, and metric evaluation, and is designed to rapidly incorporate new methods and datasets. SACCELERATOR currently includes 22 SAC methods applied to 15 datasets spanning 9 technologies and diverse tissue types. Our analysis revealed substantial limitations in the generalizability and reproducibility of SAC methods across tissues and platforms. We also demonstrate that anatomical labels commonly used as ground truths are often biased, potentially error-prone, and, in some cases, unsuitable for benchmarking efforts.

Rather than scoring and comparing methods, we propose a consensus-guided workflow that aggregates clustering results to generate consensus representations. Descriptive spatial metrics highlight areas of high entropy where method disagreement is highest, enabling targeted feedback for tissue experts. Applied to brain and cancer datasets, this approach uncovered biologically meaningful patterns overlooked by individual methods and manual annotations. Our results underscore the need for iterative, expert-in-the-loop analysis and reveal that traditional evaluation metrics do not always capture the subjective qualities of results. By improving tissue annotation and addressing key benchmarking limitations, SACCELERATOR provides a robust foundation for advancing spatial omics research.

Keywords: spatial transcriptomics, clustering, ground truth, benchmark, meta-analysis, expert-in-the-loop

Introduction

Spatially resolved transcriptomics (SRT) technologies map gene expression while preserving the spatial architecture of tissues, offering insights into how cells are organized into higher-order anatomical structures, such as tissues and organs [1, 2]. Delineating higher-order anatomical structures is pivotal for advancing our understanding of biological systems. These structures reveal how cells communicate within and between tissues, offering new perspectives on the mechanisms underlying both healthy and diseased states. Such insights are critical for identifying the origins of tumor-suppressing or -promoting microenvironments, discovering biomarkers, and informing the development of targeted therapies [3]. In the brain, the intricate cellular relationships between anatomical structures, cell types, and functional circuits remain poorly understood. Leveraging SRT data to map these relationships lays the groundwork for developing comprehensive and multimodal brain atlases, bridging molecular and functional insights at unprecedented resolution [4].

Since 2020, more than 50 spatially aware clustering (SAC) methods have been developed to delineate the structures in SRT data into spatial regions. However, terminology describing these spatial regions remains inconsistent across studies. In some studies, "spatial domains" or "spatial clusters" are loosely defined as tissue regions exhibiting spatially coherent gene expression patterns [5]. Others characterize domains as unique local features with distinct cell-type compositions, transcriptomic heterogeneity, and cell-cell interactions [6]. Yet others use the terms "spatially homogeneous regions" [7], "cellular neighborhoods" [3], "schematics" [8] or "niches" [9] to describe regions of homogeneous cell-type composition and/or expression. However, the term "niche" has also been used to describe a local structure in tissues that can reside within a tissue region [10]. Additionally, "milieu" refers to the immediate environment surrounding a cell, encompassing its direct neighbors, extracellular fluids, and the extracellular matrix [11]. This lack of standardized terminology reflects the diversity of biological questions and spatial scales addressed by SRT, ranging from individual cells [12] to organs [13], which further complicates method comparison and downstream analysis. It is important to distinguish between (i) the well-established anatomical structures (e.g., "Functional Tissue Units" [14] or parcellations [15]), (ii) the computationally identified features, and (iii) the modeling approaches used. SAC methods typically integrate gene expression and spatial information through feature engineering, dimensionality reduction, and clustering. However, the resulting clusters may not always align with biological structures of interest, highlighting the need for clarity in definitions and expectations.

Robust benchmarking is required to guide method selection and parameterization. Previous studies have compared SAC methods across various settings, including SRT technologies, tissues and simulated datasets, pre-processing, and random seed initializations [5, 16–18]. However, these studies are not easily extensible to new methods or datasets, and are limited in scope, focusing primarily on brain datasets generated by earlier technologies such as Visium.

The most common approach to benchmark SAC methods is to compare their output with ground truth (GT) annotations. Traditionally, these GT annotations are manually annotated based on apparent structures and regions using histological stains such as hematoxylin and eosin stain (H&E), often augmented with tissue-specific labels to visualize cytoarchitecture, pathology, or other features of interest [19]. Because GT annotations are commonly determined manually by experts, they are prone to human error and knowledge biases. The lack of well-defined ontologies describing anatomical structures in tissues hinders accurate and standardized definition of GTs, although, efforts are underway to define cell-type ontologies using single-cell and SRT technologies [20–23].

The challenges of benchmarking SAC methods became apparent during the BioHackathon Germany SpaceHack 2.0 project [24]. Our initial goal was to implement an extensible, community-driven benchmark

to quantitatively evaluate the performance of SAC methods across different SRT technologies and tissues, but we encountered three main obstacles. First, most SAC methods were not sufficiently demonstrated on modern SRT technologies. Second, the conceptual complexity in defining GTs rendered standard performance metrics difficult to interpret. Third, in most real-world scenarios, SAC methods are utilized in an interactive and iterative way, giving more importance to being able to investigate the output of different methods and parameters.

To address these challenges, we propose a consensus-guided, expert-in-the-loop framework to systematically evaluate commonalities and differences between methods and parameter choices. This framework enhances tissue annotations, facilitates method recommendations, and reflects the iterative, collaborative nature of spatial omics research.

In this study, we present evidence of inconsistencies in previously reported method performances and demonstrate the value of leveraging consensus among SAC results. We also highlight the need for improved computational efficiency in SAC methods to accommodate modern large-scale SRT datasets. Finally, we present two case studies to illustrate the utility of method consensus and entropy in expert-guided analysis. Our extensible framework, SACCELERATOR, is available on GitHub (see Data and code availability) with clear contribution guidelines and templates to enable the research community to reuse and extend the existing implemented datasets, methods, and metrics investigated in this study.

Results

Reported performance of spatially aware clustering methods is inconsistent across studies

We observed inconsistencies in reported method performances across existing SAC benchmarks. To evaluate this systematically, we conducted a meta-analysis of 13 studies [9, 12, 16, 25–34], using the widely-used Visium dataset of the human brain dorsolateral prefrontal cortex (LIBD DLPFC) region [35].

We focused on BayesSpace, a foundational SAC method, as a benchmark control. We expected relatively consistent BayesSpace results across studies; however, collected adjusted Rand indices (ARI) revealed substantial variability across studies (Figure 1A). For instance, slice 151673 showed strong and consistent performance (and is often showcased in the literature [12, 25–29]), whereas the results of slice 151669 fluctuated dramatically, highlighting the lack of robustness of reported method performances across previous studies.

As expected, we observed that performances reported in method papers are frequently higher than those reported by subsequent competitors (Figure 1B). This discrepancy could arise from the original studies optimizing their methods to demonstrate superior performance, or suboptimal parameter choices in subsequent comparisons. While neutral benchmarking studies have aimed to systematically address such biases, we still encountered inconsistencies. For example, BayesSpace was ranked as 4th out of 14 methods in Yuan et al. [5] but 13th out of 16 methods in Hu et al. [16] based on the same LIBD DLPFC dataset. Taken together, this meta-analysis questions the utility of conventional SAC benchmarks.

An extensible framework for running and evaluating SAC methods

Given the limitations of existing benchmarking efforts, we investigated the utility of SAC methods across various real-world scenarios. To achieve this, we developed SACCELERATOR, a modular and reproducible workflow built on Snakemake [36], specifically designed for straightforward extension with new datasets, methods, and evaluation metrics (Figure 1C). Within this framework, each dataset, method, and metric is

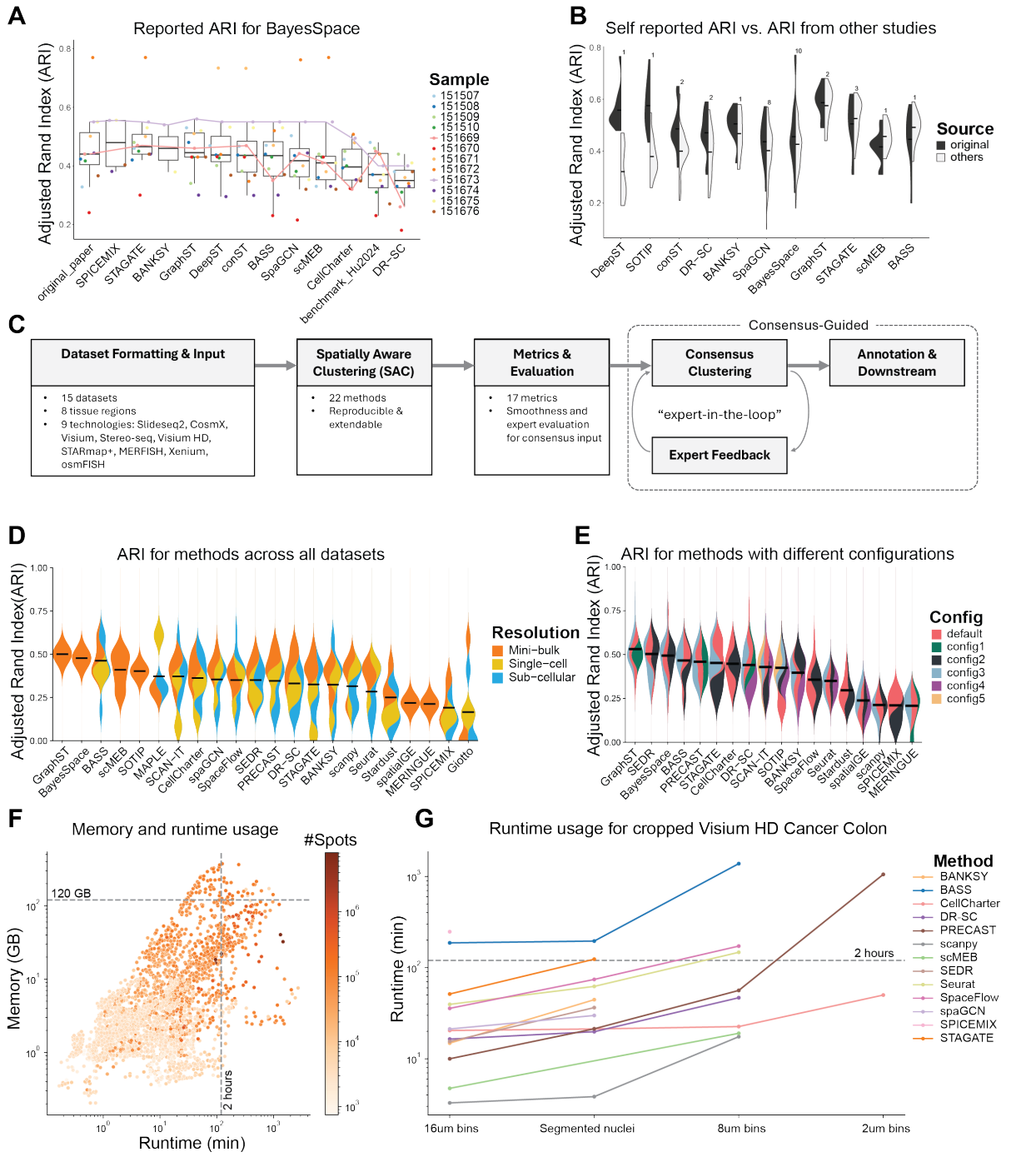

Figure 1: **Addressing inconsistent reporting of method performance. A**. Reported Adjusted Rand Index (ARI) of BayesSpace on the Visium dataset of the human dorsolateral prefrontal cortex (LIBD DLPFC), in the original BayesSpace study and other studies. The reported ARI for each sample in the dataset is depicted in a different color, with those for slices 151669 and 151673 connected with a line. Studies after BayesSpace are ordered by decreasing median ARI. **B**. The original self-reported ARI (dark grey) vs the ARI reported in other studies (light grey) for method performance on the LIBD DLPFC dataset. Methods are arranged by the difference of mean self-reported ARI vs those in other studies. **C**. Schematic of the SACCELERATOR framework. **D**. ARI for methods across different spatial resolutions of SRT technologies. **E**. ARI for methods using different configurations applied to the LIBD DLPFC dataset. **F**. Memory usage vs CPU runtime across SRT technologies, colored by the number of spots/cells in those datasets. **G**. CPU runtime of methods on 25% of the Visium HD colorectal cancer dataset across various bin sizes.

encapsulated as an independent module, with standardized command-line interfaces and outputs. This modular structure enables seamless integration of additional methods or datasets, and method-specific configuration files to facilitate systematic exploration of parameter spaces.

Recognizing that SRT technologies produce data in diverse formats, we defined a set of necessary and optional metadata for each dataset and systematically stored it with the SRT data in generic file formats

(TSV, JSON). This design ensures that downstream analyses are agnostic to the underlying technology and that data can be easily accessed across different programming languages.

The SACCELERATOR framework enables performance evaluation via both spatially agnostic clustering metrics, such as ARI or normalized mutual information, as well as spatially aware metrics, such as spatial chaos score [6], percentage of abnormal spots score [6], or spot entropy [37]. These spatially aware metrics consider the spatial location of the predicted labels and/or evaluate the spatial continuity of the clusters [6, 37, 38]. Moreover, the clustering results of different parameter combinations or multiple methods can be aggregated and leveraged for analyses using consensus clustering approaches (more on this below).

Our current implementation includes data from over 170 tissue samples from 15 datasets, generated using sequencing-based SRT technologies Visium [39], Visium HD [40], Slide-seqV2 [41], and Stereo-seq as well as the imaging-based technologies Xenium, CosMx, STARmap PLUS [42], and MERFISH [43] (See Methods, Table 1 for dataset summaries). Technologies were grouped by spatial resolution as mini-bulk (Visium), single-cell (Slide-seqV2, Visium HD), or sub-cellular (Stereo-seq, Xenium, CosMx, STARmap PLUS, and MERFISH). The framework applied the 22 implemented methods (Supplementary Table S1) to these datasets, each with one to four parameter configurations (61 total combinations; Supplementary Table S2). The method outputs were evaluated using 17 different metrics that used the GT labels and spatial information to varying extents (Supplementary Table S3). In general, we observed substantial variation in SAC method performance as measured by ARI (Figure 1D). Conversely, most evaluation metrics showed high similarity (Supplementary Figure S2).

Method-specific parameter choices, such as the number of principal components or the degree of smoothing, can contribute to performance variability. To assess the impact of parameterization, we evaluated each method using both default settings and parameters recommended in tutorials or dataset-specific analyses after uniform application of quality control and filtering steps (see Methods). Our results indicate that differences between parameter configurations can exceed those between different methods (Figure 1E). Some methods exhibited stable performance across configurations (e.g., GraphST and CellCharter), while others (e.g., STAGATE) achieved results ranging from top- to bottom-tier performance, likely reflecting sensitivity to technology-specific parameters (Figure 1E). This pronounced sensitivity underscores the challenge for users in selecting optimal settings and highlights the need for clear guidance and robust defaults.

As a community-driven resource, SACCELERATOR is designed for ongoing expansion, and we encourage users and developers to contribute additional datasets and methods (see Data and code availability for a link to the framework and guidelines).

Few current methods scale to modern datasets

Newer SRT technologies have improved spatial resolution and/or gene plexity, leading to a substantial increase in data volume. The smallest dataset we evaluated contained fewer than 3,500 spots (Visium LIBD DLPFC), while the largest dataset contained more than 460,000 cells (CosMx liver cancer). To assess whether SAC methods scale to large datasets, we applied them to large Visium HD, Stereo-seq, Xenium, and CosMx datasets. We measured the CPU runtime and memory usage of the methods with respect to the number of spatial observations (i.e., cells/bins/spots) and features (genes). We found that both runtime and memory usage increased exponentially with the number of spatial observations (Figure 1F), whereas the number of features had little impact, likely due to the widespread use of feature selection and/or dimensionality reduction steps in most SAC methods (Supplementary Figure S1A). Similarly, the specific SRT technology had less impact on runtime and memory usage than the number of spatial observations (Supplementary Figure S3).

Most methods scaled well until 200,000 spatial observations (Figure 1F), but only 5 of 22 methods were able to process the largest dataset (CosMx liver cancer) on a compute node with 500 GB RAM and 10 cores within 2 days.

To further explore method scalability, we examined resource usage for the Visium HD colorectal cancer dataset across multiple bin-sizes (2, 8, 16 µm, resulting in 8, 0.5, and 0.125 million bins, respectively) (Supplementary Figure S1B). While 11 out of the 22completed for the 16 µm bins, only 5 could process the 8 µm bins, and just CellCharter managed to process the 2 µm bins within the memory and runtime constraints; all other methods exceeded the 500 GB memory limit. Since only one method completed for all bin sizes, we repeated the experiment using a cropped 25% subset of the dataset (Figure 1G). This increased the number of methods able to process the 16 µm bins to 13 (of 22), and 8 successfully finishing for the 8 µm bin. For the smallest bin size, only PRECAST could now successfully run in addition to CellCharter. Of these two, CellCharter demonstrated both lower memory usage and faster runtime. When comparing the resulting clusters to each other and to the ground truth, the two methods showed low similarity (ARI = 0.10), with CellCharter being more similar to the ground truth than PRECAST (ARIs = 0.31 vs 0.07; Supplementary Figure S4).

Taken together, these results demonstrate that most SAC methods do not currently scale to state-of-the-art SRT technologies and may not be usable for large-scale analyses, such as those involving large cohorts or extensive tissue sections.

Over-reliance on ground truth annotations complicates method evaluations

One of the principal limitations affecting the validity of benchmarking studies for SAC methods is the reliance on GT labels. GT labels are often derived from multi-modal information, which may not be fully reflected in the transcriptome alone. For example, in the Visium LIBD DLPFC dataset [35], GT annotations were generated by cross-referencing histological H&E staining images (Figure 2A) with marker gene expression. Except for white matter and, to a lesser extent, layer 6, the brain isocortex layers in this dataset were grouped closely in the first two principal components based solely on transcriptional profiles (Figure 2B).

Gene expression differences across the isocortex layers were subtle and could be further obscured by technical limitations, such as coarse resolution (multiple cells per spot), transcript-capture biases (e.g., lateral diffusion), and other technical limitations of sequencing-based SRT technologies [44]. Beyond these technical challenges, there may be conceptual misalignments between the identified spatial clusters and the biological reality of tissue organization. Many biological phenomena, including transcriptomic variations, gradient-driven expression patterns (see thalamus case study below), and transitional cell stages, are continuous and diffusive processes, whereas spatial cluster detection inherently discretizes the landscape.

The assignment of GT labels is also inherently subjective, typically reflecting the annotator's biological interests and the scale of their investigation. For instance, in the Xenium mouse brain datasets (Datasets, Figure 2C), the entire isocortex is labeled as a single region in the GT (Figure 2D; highlighted in box). However, when methods were configured to identify the same number of clusters as the GT labels, some methods detected more refined, layered structures within the isocortex (Figure 2C; 11 clusters, Supplementary Figure S5). Although these layered structures in the isocortex are biologically meaningful, they diverge from the GT label delineations and result in lower ARI scores. Conversely, configuring methods to find fewer clusters (Figure 2C; 7 and 9 clusters) produces a less granular isocortex structure that better matches the GT labels and yields higher ARI scores (Figure 2E; green). However, this reduction in granularity can obscure other important anatomical features, such as the distinction between thalamus and hypothalamus, which is

only captured at higher cluster numbers. As a result, the subjectivity of GT labels often penalizes alternative clustering strategies and induces granularity bias where methods often achieve peak ARI against the GT at cluster counts different from that of the GT labels (Figure 2 E, G, I). This phenomenon is pervasive across datasets and methods.

The challenges of using GT labels to evaluate SAC methods stem from both subjective granularity and divergent annotation objectives. For example, the GT annotation for the Visium breast cancer dataset [45] (see Datasets, Figure 2F) consists of four manually defined regions: tumor, tumor-surrounding, invasive, and healthy tissue. While these labels provide a biologically motivated scaffold, their coarse granularity introduces evaluation biases, where methods such as STAGATE and SCAN-IT achieve their highest ARIs only when configured to identify more clusters than those defined in the GT label (Figure 2G). More fundamentally, there exists an intrinsic mismatch: GT labels are annotated to capture broad pathological zones based on visual histological features, whereas most SAC methods are optimized to identify transcriptionally coherent spatial patterns. This conceptual disconnect leads to uniformly low ARI scores across all methods (mean ARI = 0.20), even when the resulting clusters visually correspond to meaningful tissue structures (Supplementary Figure S6).

In the Stereo-seq mouse liver dataset [45] (Figure 2H, see Datasets), the GT labels were annotated to reflect hepatocyte zonation patterns between central and portal veins in liver lobules [46]. While zonation patterns represent physiologically relevant processes, most SAC methods achieved a low ARI score for this dataset (Figure 2I, Figure S7). This low ARI could potentially be attributed to several factors, including the use of supervised gene selection for GT annotation or the granularity of the annotated zones.

To assess the impact of expert gene selection, we identified 925 zonation-associated gene sets from three studies [47–49] that were not used during the original annotation of the Stereo-seq mouse liver dataset. This had mixed effects on the results, with SpaceFlow achieving high ARI and SEDR and CellCharter reporting lower ARI compared to their performance based on all genes (Supplementary Figure S8).

We further investigated the effect of annotation granularity. The original GT divided the zonation pattern into nine equal parts, but these could also be grouped into three biologically established layers: pericentral, midzonal, and periportal. When using this three-layer level of granularity, ARI scores improved markedly compared to the original nine-layer GT (Figure 2H, I), highlighting the importance of matching the granularity of GT labels to the biological structures of interest. This also suggests that some SAC methods may benefit from leveraging expertly defined gene sets rather than relying solely on unsupervised gene selection.

Since manually annotating GT labels is a challenging and time-consuming process, some datasets have used computationally generated GTs (Table 1). For example, in the Stereo-seq mouse embryo dataset, GT labels were derived using Spatially Constrained Clustering, a method building on the Leiden algorithm [13]. This methodological overlap likely explains why Leiden clustering implementations in Seurat and Scanpy achieved the highest mean ARI scores (0.428 and 0.421, respectively; Supplementary Figure S9). The use of computationally determined GTs introduces circularity, which is also evident in SAC benchmarking studies of the STARmap mouse cortex dataset. BASS, the method used to generate GT labels, consistently achieved top-tier performance in neutral benchmarks [5, 16].

Collectively, these challenges, such as discretization of continuous processes, granularity bias, circularity, and technical artifacts, are pervasive across current GT labels used in SAC benchmarking. While careful curation may mitigate some issues, the inherent limitations of GT labels still undermine their reliability, and consequently, the validity of current benchmarking practices.

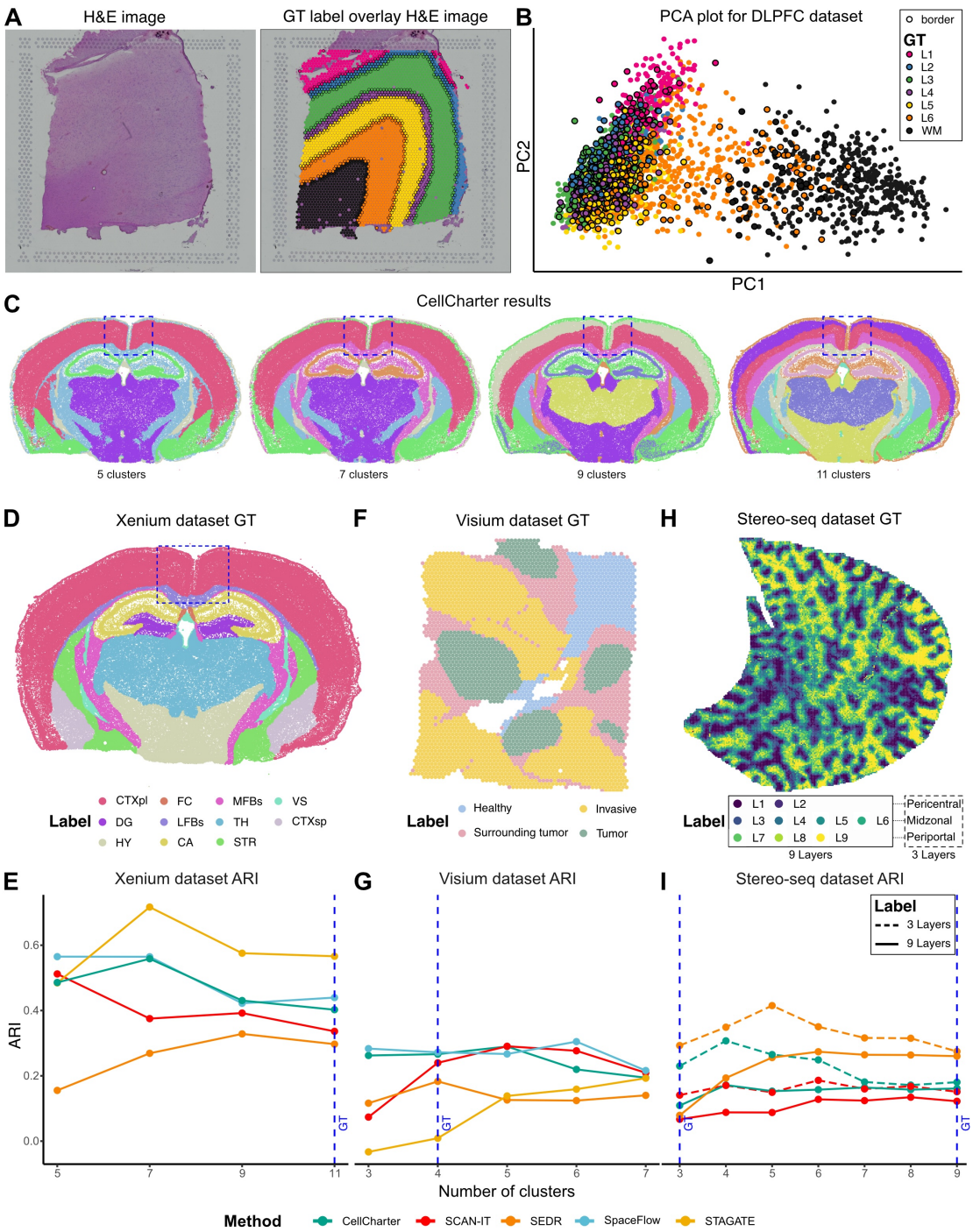

Figure 2: **Challenges in utilizing ground truths effectively for benchmarking. A**. H&E images of dorsolateral prefrontal cortex from the Visium LIBD DLPFC Br8100_151673 slice (left), and the ground truth (GT) annotation of the same sample overlaying on the H&E image (right). **B**. LIBD DLPFC Br8100_151673 slice, projected on the 1st and 2nd principal component (PC), colored by GT labels. Spots that are spatially located at the border between GT clusters are marked with black outlines. **C**. The results of CellCharter on the same sample while setting the number of clusters to 5, 7, 9, and 11. **D**, **F**, **H**. Spatial plots of the GT labels of Xenium mouse brain dataset (**D**), Visium Breast Cancer dataset (**F**), and of Stereo-seq mouse liver dataset (**H**). **E**,**G**,**I**. ARI against the GT labels of several methods when set to identify varying numbers of clusters for the corresponding Xenium (**E**), Visium (**G**), and Stereo-seq (**I**) datasets. The cluster number of the GT labels is marked by dashed blue lines. Two sets of GT labels are shown in the Stereo-seq dataset (**I**), marked by different line types. GT: Ground truth, ARI: Adjusted Rand Index.

Methods are often more similar to each other than to the ground truth

Given the challenges in effectively utilizing GT references, we explored the similarity of clustering results produced by different SAC methods. We compared "base clusterings" (i.e., the set of clustering results from the multiple configurations of multiple methods) to each other and also computed smoothness entropy (SE;

see Methods) as an intrinsic, GT-independant performance measure, since some level of spatial continuity of clusters is expected.

For the Visium LIBD DLPFC dataset, base clusterings revealed a wide range of smoothness levels (Figure 3A, B; Supplementary Figure S10). SAC methods often exhibit higher concordance with each other than to the GT (Figure 3B). Notably, for slice 151673 of the LIBD DLPFC dataset, we identified a block of base clusterings with method-vs-method ARIs averaging around 0.56 (Figure 3B, blue box), and another block of methods exceeding 0.62 (Figure 3B, pink box with dashed lines). This pattern of method concordance was consistent across several algorithms and all slices of the LIBD DLPFC dataset (Supplementary Figure S11).

To determine whether combining outputs from methods with both high concordance (high pairwise ARI) and spatial continuity (low SE) could yield biologically relevant groupings, we selected a subset of SAC methods (see Methods for criteria) and formed a consensus clustering using latent class analysis (LCA) [50]. LCA was chosen for its scalability to large datasets, although K-modes and weight-based consensus approaches [51–53] were also implemented in the pipeline and can be applied based on dataset characteristics. We then applied a leave-one-out strategy among the pre-selected continuous and concordant methods (Figure 3B, blue box). For each method, we built consensus clusterings using all remaining methods, which then served as a pseudo-GT to compare the method to. Comparing this leave-one-out consensus gives a readout of whether a method returns a significantly different clustering from other methods. While this is not meant to serve as a *bona fide* performance metric, clusterings that correspond well to pseudo-GTs also exhibit correspondence to the manual annotation (Figure 3C).

A by-product of consensus clustering is that we can spatially visualize where commonalities and uncertainties in base clusterings lie, for example, using a cross-method entropy (CME; lower values highlight concordance across methods; see Methods). To illustrate, we selected the 12 lowest-SE concordant-block base clusterings with seven clusters (Supplementary Figure S12) and generated a consensus clustering for slice 151673 of the LIBD DLPFC dataset (Figure 3B consensus_lca). While the human brain structure of the LIBD DLPFC dataset is known to exhibit a layered structure, we included base clusterings without perfect layering (Supplementary Figure S12). Despite the inclusion of these imperfect clusterings, the consensus exhibited a smooth (SE = 0.17) and a mostly layered cluster organization (Figure 3B). To understand areas of disagreement, we visualized the CME across the set of base clusterings (Figure 3D). Compared to the GT, many heterogeneous regions align with the boundary regions marked by both consensus and anatomical labels. Additionally, while none of the methods were able to identify cortical layer 4 (L4) in this sample (Figure 3B Annotation, purple cluster), overlapping the L4 spots with the CME plot shows that the L4 layer aligns with a high entropy region, indicating the difficulty of correctly capturing this boundary based on transcriptional data at Visium resolution.

Furthermore, we can sweep across the number of clusters and the number of base clusterings (again prioritizing the most spatially continuous) to inform analysts about common structures found across granularities. Figure 3E highlights that 7 clusters induce the highest (average) correspondence between methods, and low CME remains stable even when selecting up to 12 base clusterings for the consensus. This approach can serve as a practical guide for an initial clustering of spatial data in the absence of a GT.

Consensus with expert-in-the-loop

In practical research settings, SAC methods are rarely applied in a purely automated manner; instead, researchers frequently work in multidisciplinary teams and interact with multiple methods and parameter

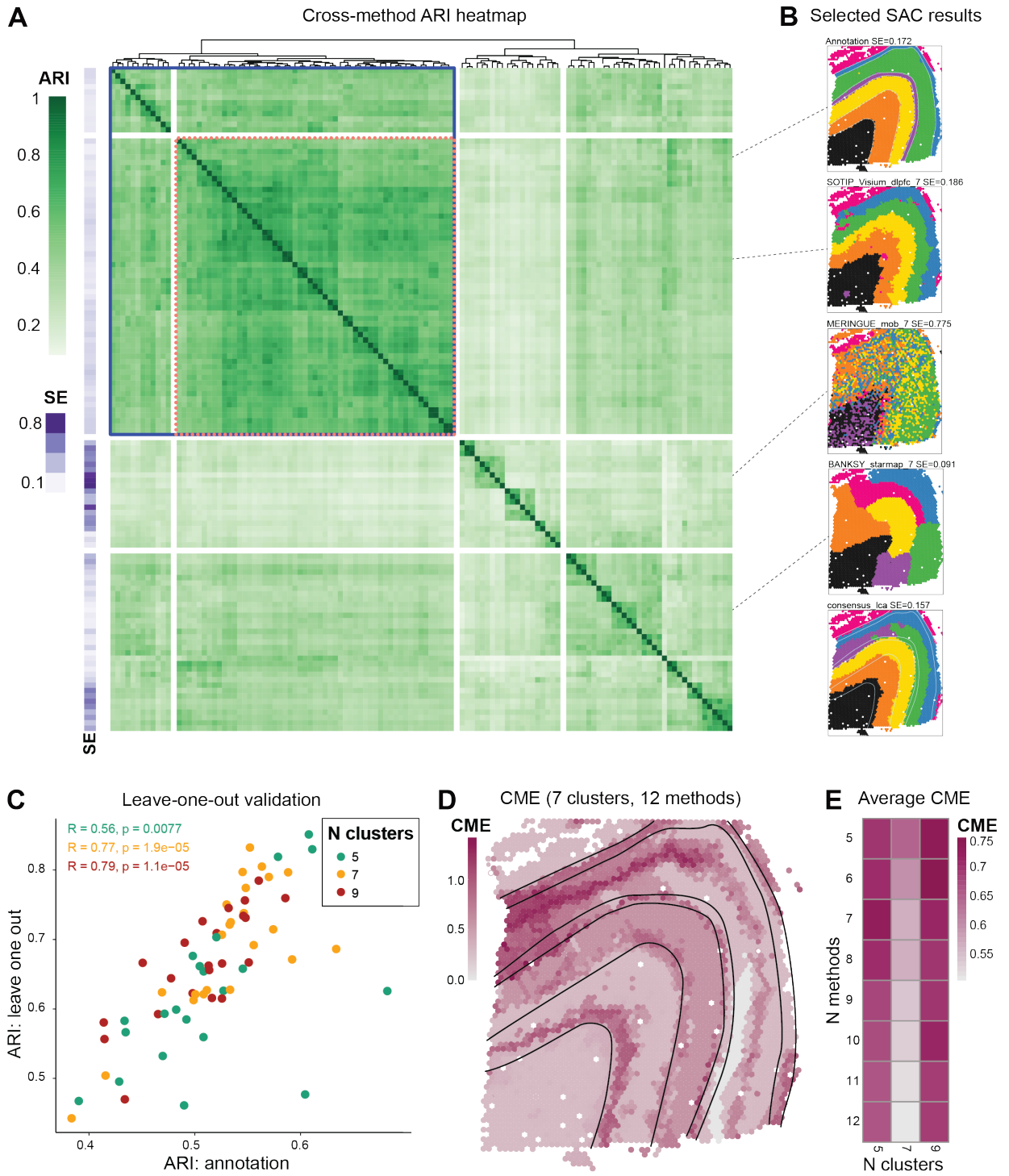

Figure 3: **Consensus and entropy of spatially aware clustering**. **A**. Method-vs-method ARIs for 119 base clusterings (including the manual annotation). The row annotations show the smoothness entropy (SE) (lower SE means 'smoother' domains or, specifically, fewer total boundaries between domains). **B**. Selected base clusterings. consensus_lca denotes a consensus clustering built from the 12 methods at 7 clusters shown in panels **D** and **E** (see Methods). **C**. ARI of SAC methods calculated against a leave-one-out consensus versus the ARI against the original ground truth annotations. **D**. Cross-method entropy (CME; spot-wise similarity of cluster membership across methods) for 7 clusters and the 12 smoothest non-duplicated SAC methods. **E**. CME (averaged over all spots) for combinations of the number-of-smoothest-methods and number-of-clusters.

settings, iteratively evaluating their outputs to select those that best address specific biological questions. The consensus clustering and parameter sweeps integrated into our framework are designed to mimic this common research workflow, enabling biologists to systematically evaluate and compare a broad range of SAC method results within a unified environment. To demonstrate the utility of this approach in a real-world context, we collaborated with domain experts to evaluate SAC method performance on two modern SRT

datasets: a MERFISH dataset of the adult mouse brain thalamus [4] and a Visium HD dataset of human colorectal cancer [54] (see Datasets).

Case study 1: Consensus SAC identifies anatomical boundaries in mouse thalamus

In the adult mouse brain, researchers have parcellated the thalamus region into approximately 40 anatomical labels, known as thalamic nuclei (Figure 4A), based on cytoarchitecture (cell shape, size, and density) and histochemical stains. However, this level of granularity is insufficient to capture the finer topographical patterns of neuronal connectivity and function that are known to exist within the thalamus [55].

SAC methods have the potential to identify novel, functionally relevant parcellations based on the information-rich and reproducible data of single-cell SRT. However, the results of eight SAC methods on the mouse thalamus MERFISH dataset showed a high level of discordance (Supplementary Figure S13). Without further refinement, this lack of agreement would only introduce confusion, rather than improve our understanding of molecular thalamic organization. Therefore, we leveraged our consensus clustering and SAC entropy analyses to interpret and apply the outputs of SAC methods on the same SRT dataset.

We compared the SAC results with each other and to the reference anatomical labels from the Allen Mouse Brain Common Coordinate Framework (CCFv3) [56] using pairwise ARIs (Figure 4B). Consistent with our findings in the Visium LIBD DLPFC dataset, we found that SAC methods tended to agree more with each other than with the anatomical reference labels (Figure 4A, B). This reiterates the limitations and risks of using anatomical annotations as GT for SAC evaluation.

Expert reviewers compared the resulting clusterings to both the reference anatomical labels and their domain knowledge of thalamic biology. The CME plot (Figure 4C) revealed regions of the thalamus that exhibited good agreement between SAC methods, as well as regions where the agreement was poor. High entropy (low cross-method agreement) frequently occurred near the boundaries between different anatomical labels. Two key insights emerged from this analysis. First, boundaries between thalamic nuclei often correspond to transitions in gene expression profile, and the entropy plot visually highlights how small differences in method choice or parameter setting can lead to variation in SAC calls at these transitions. Second, the entropy-indicated border helped us identify regions where the reference anatomical labels could be refined. While the MERFISH data was spatially registered to a whole brain reference coordinate space (CCFv3) to obtain the reference anatomical labels, this process is imperfect and results in misalignments, which are most notable at the borders between anatomical regions. The ventral posteromedial nucleus (VPM) is one example where the expression profile of key marker genes in the VPM (Figure 4D) aligns better with the entropy-indicated border than the boundaries from anatomical reference labels (Figure 4C-D; denoted by arrowheads).

We next generated consensus clusterings for the thalamus (Figure 4E-H). By sweeping the number of clusters from 16 to 24 (Figure 4E), we found cluster size and continuity to stabilize around 20 clusters, while higher cluster numbers resulted in more small and noisy clusters. We then generated consensus clusterings using three aggregation methods (LCA, weight-based, and K-modes), each set to 20 clusters (Figure 4F-H). Expert evaluation of these consensus clusterings revealed distinct behaviors among the aggregation approaches. K-modes consensus subdivided many anatomical labels into multiple clusters and introduced a high number of salt-and-pepper (non-contiguous) clusters spread across two anatomical regions: the zona incerta (ZI) and the reticular thalamic nucleus (RT). This is consistent with additional transcriptional diversity and spatial structure observed within these areas [57, 58]. This stands in contrast to the weight-based and LCA consensus clusterings, which found one cluster each for ZI and RT.

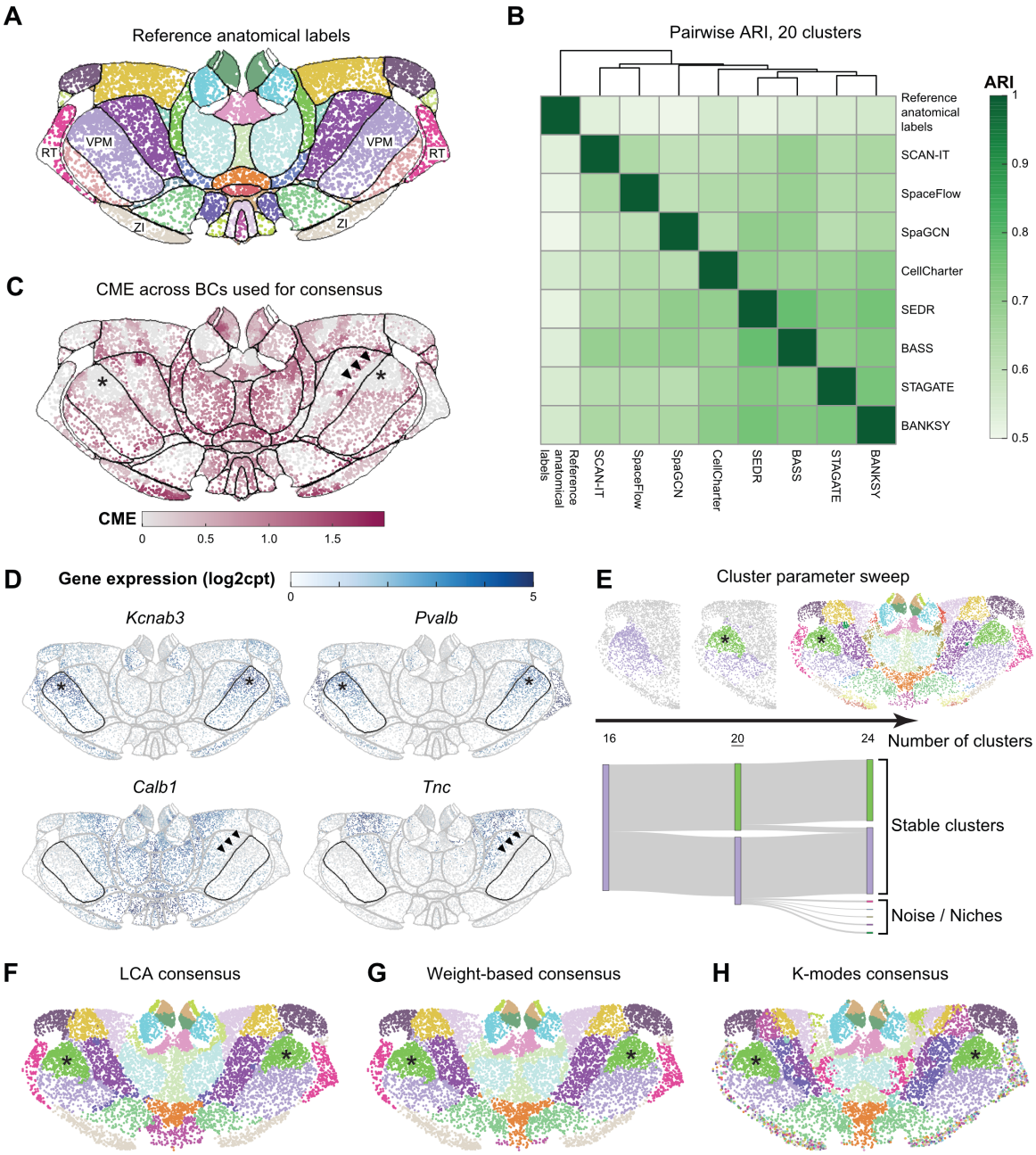

Figure 4: **MERFISH dataset of the adult mouse brain thalamus region**. **A**. Reference anatomical labels with borders indicated in black. VPM: ventral posteromedial nucleus; RT: reticular thalamic nucleus; ZI: zona incerta. **B**. Pairwise method-vs-method ARI comparison heatmap of the eight base SAC methods and the reference anatomical labels. **C**. Cross-method entropy (CME) of the eight base SAC results selected to build the consensus clusters. Reference anatomical label borders are indicated in black. Asterisks mark a low-entropy subdivision of VPM. Arrowheads mark a discrepancy between the reference anatomical borders and the SAC consensus in the right hemisphere. **D**. Gene expression of four genes (*Kcnab3*, *Pvalb*, *Calb1*, *Tnc*) that have spatially variable expression within or at the boundaries of the VPM subregion of the thalamus. The borders of all reference anatomical labels are outlined in grey; VPM is highlighted in black. **E**. Weight-based consensus of the datasets for 16, 20, and 24 clusters, with left VPM structure highlighted for the 16 and 20 cluster cases (top). 20 clusters (underlined) was used to generate the consensus clusterings in (**F-H**). Sankey diagram of the VPM region with the increase of cluster number (bottom). **F**. Consensus clustering computed with Latent Class Analysis (LCA) and clustering parameter set to 20 clusters. **G**. Consensus clustering computed using a weight-based framework and clustering parameter set to 20 clusters. **H**. Consensus clustering computed using K-modes and clustering parameter set to 20 clusters. Data from Yao et al. [4]; downloaded from the Allen Brain Cell Atlas.

Interestingly, we observed that some anatomical regions were consistently subdivided by all three consensus methods. For example, VPM was split into two clusters (Figure 4F-H; denoted by asterisks), reflecting the multi-gene expression gradients in the SRT data (Figure 4D; denoted by asterisks). The genes shown were chosen based on differential expression between the cells in the two VPM clusters (Methods) and may correspond to the spatial organization of neurons in VPM based on their axonal projections [59]. Given the high interest in identifying novel molecular parcellations of the thalamus, this robust consensus approach,

combined with reassurance that we can find a stable number of clusters, is a promising target for subsequent experimental investigation with additional molecular and multimodal measurements.

Case study 2: Detecting neoplastic progression stages in colorectal cancer

To evaluate our approach in a setting lacking established anatomical reference labels, we analyzed a previously unannotated SRT dataset of a pre-treatment human colon adenocarcinoma specimen sample profiled using Visium HD [54]. To incorporate domain expertise, we engaged both a histologist (A.E-H.) and a pathologist (M.Z.) specializing in colorectal cancer, who provided iterative feedback throughout the analysis process. This use case reveals another aspect of cluster annotation: a pathologist may not be equally interested in all regions, instead focusing their attention on pathophysiologically distinct areas.

Initially, the histologist annotated the tissue sections based on a high-resolution H&E image. The neoplasm (regarded as tumor tissue in this sample) boundary was then refined using *EPCAM* expression (Supplementary Figure S16), consistent with established FISH workflows (Figure 5A). These annotations served as a baseline for evaluating the performance of the SAC methods applied to the dataset. We observed a clear correspondence between expert annotation and the SAC results (Supplementary Figure S14), with a consistent difference being the split of the area annotated as neoplasm into two distinct clusters (Figure 5B). Only a subset of algorithms were able to process the dataset at full resolution (2 µm bins) due to memory and runtime limitations (Figure 1G), which limited our analysis to the 16 µm bin resolution. Before analyzing ARI scores, the two experts independently ranked each algorithm based on its ability to detect relevant tissue features, including: (i) distinguishing cancer from non-cancer tissue, (ii) identifying neoplastic differentiation, (iii) differentiating between all colon tissue compartments, (iv) identifying lymphovascular and perineural structures, (v) detecting small groups of neoplastic cells, (vi) identifying immune cells, and (vii) phenotyping of connective tissue (Figure 5C). Interestingly, this expert ranking differed substantially to the ARI scores calculated against the GT labels defined by the experts themselves (Figure 5D). DR-SC and STAGATE received the highest expert score while performing average in the ARI scoring, whereas the best-performing methods in the ARI metric, Seurat and CellCharter, did not reach the top rank as assigned by the experts. SEDR ("dlpfc" configuration) received the same rank as SCAN-IT, although the latter achieved a much higher ARI (Figure 5D). This finding is consistent with previous results and highlights the limitations of global metrics, such as ARI, in evaluating performance for small, biologically relevant structures [60].

Further investigation of nuclear morphology in the two distinct neoplasm clusters (Figure 5B, arrows) indicated a possible transition between tissue areas presenting neoplastic and dysplastic changes, characterized by increased nuclear-to-cytoplasmic ratio and nuclear crowding [61]. Annotation of these areas is usually carried out based on morphology [62], while more fine-grained molecular assessment of neoplastic cells has only recently emerged [63]. Thus, this sub-clustering of the neoplasm represents different scales of biologically relevant features that can be missed when rigidly evaluating the performance of SAC methods against manually annotated GTs.

To assess whether SAC methods could assist with this task, we subset the data to contain only bins in the neoplasm (based on the initial expert annotation) and re-applied available methods using default configurations. In the absence of a reliable way to delineate the neoplasm and dysplasia in the GT, we formed a consensus from methods showing a high concordance in terms of pairwise ARIs, reasoning that this could pinpoint pathological structures of interest (Supplementary Figure S15). Agreement between methods was generally high, as indicated by low entropy, with the exception of the boundary between tumor stroma and healthy epithelium (Figure 5G), which was the main area of disagreement between SAC methods. This

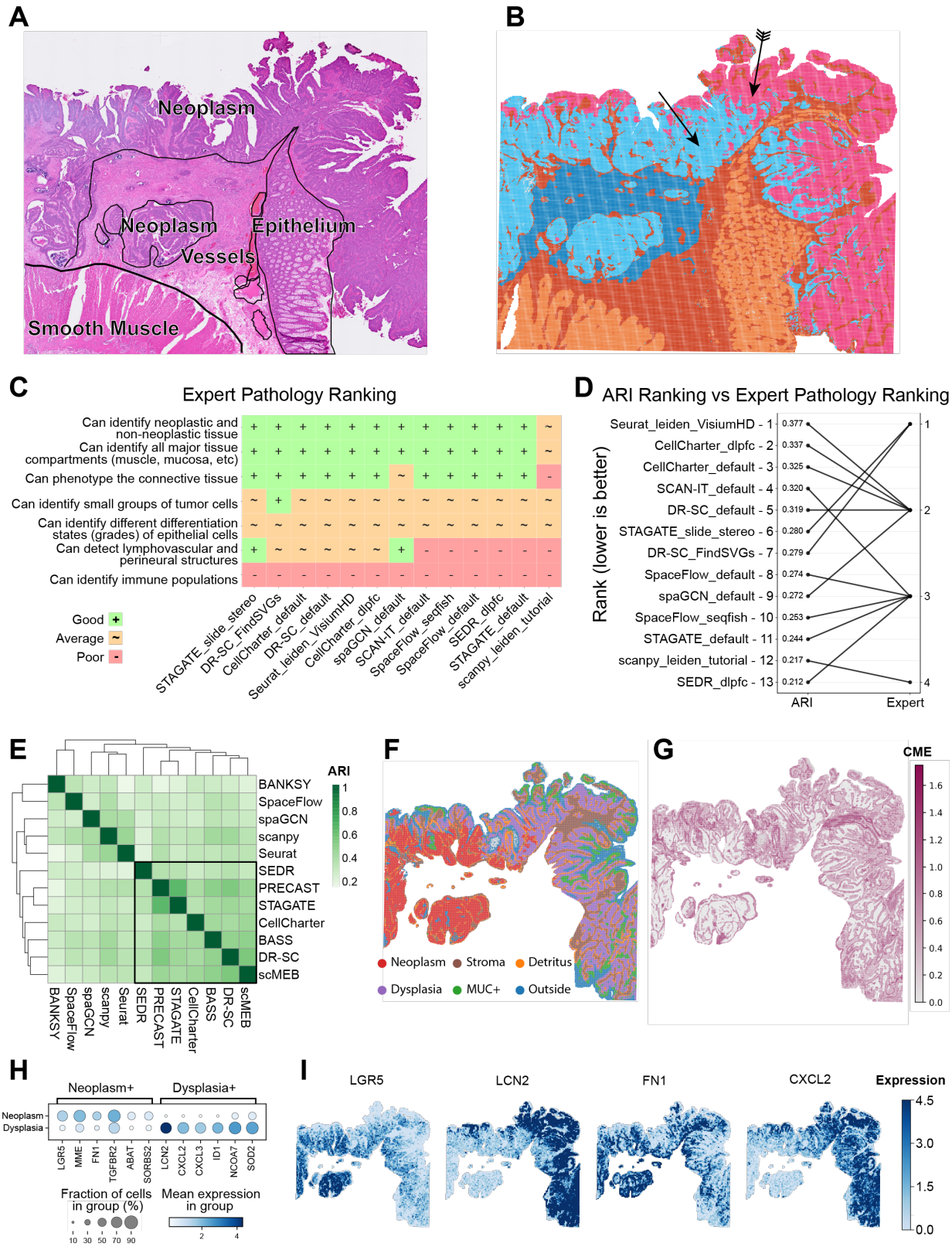

Figure 5: **Colorectal cancer Visium HD Consensus with expert in the loop. A**. Initial annotation of tissue regions based on the H&E image by an expert histologist. **B**. SEDR clustering (6 Clusters) identifies two distinct clusters in the dysplastic epithelium (feathered and smooth arrow). **C**. Expert ranking of SAC method performance for spatial feature identification relevant for pathological assessment (9 Clusters, full result can be found in Figure S14). **D**. Comparison of the ARI calculated based on annotations in panel **A** vs the expert ranking in panel **C** for each SAC method. **E**. Method-vs-method ARI comparison heatmap for the neoplasm area. The boxed methods were identified as a concordant cluster based on Euclidean distance. **F**. Consensus clustering computed using K-modes for the 7 methods highlighted in panel **E**. **G**. Cross-method entropy map of the consensus clustering. **H**. Top differentially expressed genes between neoplasm and dysplasia. Color-coded by log1p normalised gene expression and size-coded by percentage of bins expressing the gene in the clusters. **I**. Spatial expression patterns of selected genes. Expression in log1p normalized counts.

might be caused by transitional zones, similar to what was observed in case study 1. The six distinct regions identified included (i) separate tumor and (ii) dysplastic zones, (iii) mucin signaling hotspots (glycoprotein-rich areas linked to specific colorectal cancer phenotypes [64]), (iv) tumor stroma, (v) cellular detritus split off from the tumor, and (vi) an external region (likely diffusion artifacts) outside the tissue (Figure 5F).

We found several well-studied differentially expressed genes between neoplastic and dysplastic areas (Figure 5H-I). The neoplasm showed high expression levels of *LGR5* (stem cell marker gene, investigated as a therapeutic target in CRC) [65], *FN1* (extracellular matrix remodeling) [66], and *TGFBR2* (conditional tumor suppressor/activator as part of TGFβ signaling) [67]. Conversely, the suspected dysplasia was characterized by the expression of *CXCL2/3* (inflammatory markers) [68], *LCN2* (a secretory protein potentially acting as a tumor suppressor in colorectal cancer) [69], and *SOD2* [70] and *NCOA7* [71] (stress response genes). Collectively, the gene expression patterns support the transition from a premalignant, inflammatory, and stressed dysplasia to a proliferative neoplasm with pro-invasive traits.

Our findings illustrate the value of an expert-in-the-loop approach where data-driven clusters combined with domain knowledge guide method selection and analysis direction, leading to biologically meaningful and novel insights. Notably, the experts did not initially set out to investigate the dysplasia to neoplasia transition - an observation that underscores the iterative and exploratory nature of investigating tissue architecture. Their understanding evolved as they interacted with the results, highlighting the importance of flexibility in clustering approaches. Taken together, this experience suggests that defining a single GT for spatial regions is often impractical, especially in complex tissues where biological heterogeneity and functional gradients are expected.

These case studies challenge the traditional paradigm of benchmarking SAC methods solely against fixed reference labels and emphasize the necessity of context-specific evaluation. They demonstrate that SAC methods can capture a spectrum of biologically relevant patterns, revealing insights that may be overlooked by rigid, single-label GTs. By embracing this multiplicity of interpretations, we can better leverage the full potential of SRT to uncover novel tissue architectures and disease mechanisms.

Discussion

Existing benchmarks of SAC methods have generally focused on older SRT technologies and brain tissue datasets, often depending on questionable GT annotations or specific annotation scales, limiting the generalizability and real-world applicability of their results. To address these limitations, we developed SACCELERATOR, a consensus clustering framework designed to better reflect realistic research workflows, where researchers iteratively analyze data and work in multidisciplinary teams to interpret and refine findings. By integrating consensus of base clusterings with spatial metrics that highlight areas of high entropy (method disagreement), our approach enables targeted feedback for tissue experts. When applied to brain and cancer datasets with expert-in-the-loop evaluation, SACCELERATOR revealed biologically meaningful patterns that were previously overlooked, demonstrating that traditional evaluation metrics do not always reflect the subjective quality of results.

Our meta-analysis of reported performances across studies revealed considerable inconsistencies, highlighting the unreliability of current benchmarking practices. Method performances varied widely between studies, even when using the same datasets and algorithms. This variability can be attributed to several factors, including sensitivity to parameter choices and preprocessing steps, unreliable ground truths, and technology-specific performance. In particular, the impact of parameterization and preprocessing further complicates benchmarking efforts. To better reflect real-world usability, we evaluated methods using default

settings and author-recommended technology-specific configurations rather than greedily sweeping through multiple configurations.

To date, performance evaluation of SAC methods has largely relied on metrics that assess alignment with GT labels. Our results illustrate the limitations of solely relying on such metrics, given the inherent challenges in defining GT for complex tissues. Instead, we showed that a consensus clustering approach can be used to identify reproducible clusters, i.e., those consistently identified across methods and configurations, as well as pinpoint interesting regions of method disagreement. In our case studies, high entropy between methods highlighted biologically meaningful gradients, such as the transition from dysplasia to neoplasia in colorectal cancer. Such nuanced patterns cannot be captured by a single, discrete annotation. The consensus approach also showed robust subdivisions within anatomical regions, such as the VPM nucleus in the thalamus, highlighting its potential to uncover molecular markers for functionally relevant anatomical regions, such as the organization of thalamocortical cells in VPM [59]. Although we have not exhaustively investigated all possible clustering granularities, our framework allows researchers to investigate spatial structures at multiple scales.

Consensus among computational methods has been used in biomedical research as it conceptually overcomes limitations with the lack of ground truth knowledge [72]. Also in the context of SAC, the concept of consensus clustering is not new. For example, STCC offers a range of consensus strategies for SAC base clusters [73], but in our tests, STCC did not scale beyond Visium-sized datasets. Similarly, EnSDD, which also implements ensemble strategies based on binary similarity matrices [53], is unlikely to scale to datasets from newer technologies (the methods that overlap with our study did not scale to 2-µm-resolution Visium HD datasets). Conceptually, these frameworks utilise the consensus approach to better align with the GT. By contrast, SACCELERATOR employs consensus clustering as a guide for users and, explicitly, not as a means to maximise GT alignment. Beyond their biological relevance, consensus clusterings provide valuable feedback for method developers. If their method's output diverges from the consensus, this can pinpoint unique strengths or limitations. One further aspect to note is that our consensus clustering is not using spatial information; therefore, methods from geography that impose spatial constraints may be valuable for future development [74].

As SRT technologies continue to improve in resolution and throughput, scalability becomes an increasingly critical concern. We found that many current SAC methods struggle with large datasets, particularly those from high-resolution platforms like Visium HD or imaging-based technologies capable of profiling large tissue areas. Only a small subset of methods could process the largest datasets within reasonable time and memory constraints, underscoring the urgent need for more computationally efficient SAC methods.

Although our study focuses on the use case of spatially aware clustering, the SACELLERATOR framework is generic and provides a flexible and robust foundation for advancing meaningful evaluation of computational tools in other areas of genomics research. By bridging the gap between computational analysis and biological interpretation, and by reflecting the collaborative and iterative nature of real-world scientific inquiry, our approach supports more accurate, reproducible, and biologically meaningful discoveries.

Methods

Datasets

We evaluated SAC methods across 15 published datasets representing both newer and older SRT technologies. Datasets were categorized based on their spatial resolution: mini-bulk, single-cell, and sub-cellular (Table 1). Only datasets with available GT annotations were considered for inclusion. To ensure biological relevance and technical diversity, we prioritized non-brain tissues datasets with sub-cellular spatial resolution.

The spatially resolved gene expression data, GT annotations, and further metadata were downloaded from original sources and converted to a standardized TSV/JSON format using our Snakemake pipeline. Since the datasets used in this study originate from publicly available sources that have already undergone careful curation by their respective authors, we applied minimal filtering. Specifically, we removed cells/bins with no gene expression, removed genes that were not expressed in any cell/bins, and we excluded cells in which mitochondrial transcripts accounted for more than 30% of total transcripts. For datasets generated using mini-bulk technologies, we filtered out bins containing fewer than 10 cells when this information was available. Furthermore, if the metadata contained bin-wise information of whether the bins overlapped with the tissue region, we excluded those outside the tissue area. No additional preprocessing was applied. Quality-filtered raw data were directly input into each method, following the method implementation or vignette without modification. Table 1 provides an overview of the analyzed datasets.

CosMx human liver liver dataset (cosmx_liver)

The CosMx human liver dataset was obtained from the NanoString website (https://nanostring.com/products/cosmx-spatial-molecular-imager/ffpe-dataset/human-liver-rna-ffpe-dataset). The dataset consists of 2 Formalin-Fixed Paraffin-Embedded (FFPE) samples from 2 patients, one being normal liver and the other from a hepatocellular carcinoma patient with grade G3 cancer. Data was generated on the CosMx platform using the Human Universal Cell Characterization Panel 1000 plex. The ground truth annotations were computationally identified using Mclust clustering on the frequency of each cell type among its 200 nearest neighbors.

CosMx human non-small-cell lung cancer dataset (cosmx_lung)

The CosMx human non-small-cell lung cancer dataset was obtained from the NanoString website (https://staging.nanostring.com/products/cosmx-spatial-molecular-imager/ffpe-dataset/nsclc-ffpe-dataset). The dataset consists of 8 FFPE samples from 5 patients presenting with non-small-cell lung cancer grade G1-G3. Data was generated on a CosMx prototype instrument using a 960 gene panel [75]. The ground truth annotations were computationally identified using Mclust clustering on the frequency of each cell type among its 200 nearest neighbors.

MERSCOPE mouse brain thalamus (abc_atlas_wmb_thalamus)

The MERFISH mouse brain thalamus dataset [4] was obtained from the Brain Knowledge Platform (https://portal.brain-map.org/atlases-and-data/bkp/abc-atlas; https://alleninstitute.github.io/abc_atlas_access/descriptions/MERFISH-C57BL6J-638850.html). The dataset consists of 59 fresh frozen (FF) serial full coronal sections at 200-µm intervals spanning one entire mouse brain. Data was generated on a Vizgen MERSCOPE instrument using a custom gene panel of 500 genes. The ground truth annotations were

identified by aligning the MERFISH data to the CCFv3 coordinate space and labeling cells with the corresponding CCFv3 anatomical parcellation term [56]. Only the thalamus (TH; CCFv3 structure ID 549) and hypothalamic zona incerta (ZI; CCFv3 structure ID 797) were analyzed in this study. Spatially variable genes in the thalamus were identified by differential gene expression analysis on neighboring consensus clusters.

MERFISH human developmental heart dataset (merfish_devheart)

The MERFISH human developmental heart dataset [76] was obtained from Dryad (https://datadryad.org/stash/dataset/doi:10.5061/dryad.w0vt4b8vp). The dataset consists of 4 FF samples from 2 donors at 13 and 15 post-conception weeks (PCW). Data was generated using MERFISH with a custom 238-gene panel. The ground truth annotations (referred to as cellular communities in the original study) were computationally identified using k-means clustering of relative cell-type composition within 150 µm of each cell.

STARmap PLUS mouse brain dataset (STARmap_plus)

The STARmap PLUS mouse brain dataset [77] was obtained from Zenodo (https://zenodo.org/records/8327576). The dataset consists of 20 FF samples from 3 mice. Data was generated using STARmap PLUS using a custom 1,022 gene panel. The ground truth annotations were manually identified by aligning the data to the CCFv3.

Xenium human breast cancer dataset (xenium-ffpe-bc-idc)

The Xenium breast cancer dataset was obtained from the 10x website (https://www.10xgenomics.com/datasets/xenium-ffpe-human-breast-with-custom-add-on-panel-1-standard). The dataset consists of 1 FFPE sample from a patient with infiltrating ductal carcinoma breast cancer. Data was generated on a Xenium Analyzer using the Xenium human breast gene expression panel v1 (280 genes) with 100 additional custom genes. The ground truth annotation was manually identified using the matched histopathology image, annotating for eight region types: ductal carcinoma in-situ, invasive tumor, normal ducts, immune cells, cysts, blood vessels, adipose tissue, and stroma [78].

Xenium mouse brain dataset (xenium-mouse-brain-SergioSalas)

The Xenium mouse brain dataset was obtained from the 10x genomics website (https://www.10xgenomics.com/datasets/fresh-frozen-mouse-brain-replicates-1-standard). The dataset consists of 1 FF sample of a full coronal section. Data was generated on a Xenium Analyzer using the v1 mouse brain gene expression panel (247 genes). The ground truth annotation was manually identified using the mouse coronal P56 sample from Allen Brain Atlas [56] to specify anatomical regions [79].

Slide-seqV2 mouse brain olfactory bulb dataset (slideseq2_olfactory_bulb)

The Slide-seqV2 mouse brain olfactory bulb dataset [80] was obtained from the STOmicsDB website (https://db.cngb.org/stomics/datasets/STDS0000172/data). The dataset consists of 20 samples of a mouse olfactory bulb evenly spaced along the anterior-posterior axis. Data was generated using Slide-seqV2 and sequenced using paired-end reads on an Illumina Novaseq6000 instrument, targeting 200 million reads per sample. The ground truth annotations were manually identified based on the expression of marker genes.

Stereo-seq mouse liver dataset (stereoseq_liver)

The Stereo-seq mouse liver dataset [45] was obtained from the STomicsDB website (https://db.cngb.org/stomics/lista/spatial). The dataset consists of 6 FF samples. Data was generated on Stereo-seq chips and sequenced using paired-end reads on a DIPSEQ T1 instrument. The ground truth annotations were computationally identified where zonation layers were annotated based on the differences between the scores of pericentral and periportal hepatocyte landmark genes.

Stereo-seq mouse embryo dataset (stereoseq_mouse_embryo)

The Stereo-seq mouse embryo dataset [13] was obtained from the StOmicsDB website (https://ftp.cngb.org/pub/SciRAID/stomics/STDS0000058/stomics). The dataset consists of 53 FF samples from mouse embryos spanning E9.5–E16.5 with one-day intervals. Data was generated on Stereo-seq chips and sequenced using paired-end reads on a MGI DNBSEQ-Tx sequencer. The ground truth annotations were computationally identified using Spatially Constrained Clustering (SCC), which is built on top of the Leiden clustering algorithm [13].

Visium human brain LIBD DLPFC dataset 1 (libd_dlpfc)

The Visium human brain LIBD DLPFC dataset 1 [35] was obtained from the `spatialLIBD` Bioconductor package (https://research.libd.org/spatialLIBD). The dataset consists of 12 FF samples from 3 donors. The data was generated on Visium chips and sequenced using paired-end reads on an Illumina NovaSeq 6000 instrument. The ground truth annotations were manually identified based on cytoarchitecture and selected gene markers.

osmFISH mouse brain somatosensory cortex dataset (osmfish_Ssp)

The osmFISH mouse brain somatosensory cortex dataset [81] was obtained from the Linnarsson Lab website (https://linnarssonlab.org/osmFISH). The dataset consists of a single FF sample from the mouse brain somatosensory cortex. Data was generated using osmFISH using a custom 33-gene panel. The ground truth annotation was computationally identified using an iterative graph-based algorithm.

Visium human breast cancer (visium_breast_cancer_SEDR)

The Visium human breast cancer dataset, originally from 10x Genomics (https://www.10xgenomics.com/resources/datasets/human-breast-cancer-block-a-section-1-1-standard-1-1-0), was obtained from GitHub (https://github.com/JinmiaoChenLab/SEDR_analyses). The dataset consists of a single FF sample of invasive ductal carcinoma breast tissue. The data was generated on a Visium chip and sequenced using paired-end reads on an Illumina NovaSeq 6000 instrument. The ground truth annotation was manually identified based on the H&E image.

Visium chicken heart (visium_chicken_heart)

The Visium chicken heart dataset [82] was obtained from GEO (https://www.ncbi.nlm.nih.gov/geo/query/acc.cgi?acc=GSE149457). The dataset consists of 11 FF samples from four hearts at different stages of ventricular development. The data was generated on a Visium chip and sequenced using paired-end reads on an Illumina NextSeq 500/550 instrument. The ground truth annotations were computationally identified using Louvain clustering as implemented in Seurat v3.

Visium HD human colorectal cancer dataset (Visium_hd_cancer_colon)

The Visium HD human colorectal cancer dataset [54] was obtained from the 10x Genomics website (https://www.10xgenomics.com/datasets/visium-hd-cytassist-gene-expression-libraries-of-human-crc). The dataset consists of 1 FFPE sample of colorectal cancer obtained from the sigmoid colon of a patient. Data was generated on a Visium HD chip and sequenced using paired-end reads on an Illumina NovaSeq 6000 instrument.

Ground truth annotation of the Visium HD human colorectal cancer dataset

At the time of analysis, no ground truth annotation was available for the Visium HD human colorectal cancer dataset. After data download, the ground truth annotations were performed by a histologist with expertise in colorectal cancer tissues as either connective tissue, dysplastic epithelium, non-dysplastic epithelium, vessels, or smooth muscle based on the included H&E stain and the expression of the characteristic marker genes *EPCAM* (epithelial neoplasm), *VWF* (vessels), and *MYL9* (smooth muscle). The annotations were attached to individual Visium HD bins by annotation in `SpatialData` [83] with the help of the Napari interface [84].

Spatially aware clustering methods

We implemented all 22 SAC methods according to their original publications and official documentation. To ensure fidelity to method designs, preprocessing steps (e.g., normalization, feature selection) were replicated exactly as described in method vignettes or GitHub repositories. For parameter configurations, we included a "default" configuration, where we used author-predefined parameter values, with undefined parameters set via prominent tutorials or GitHub READMEs. Additional configurations were limited to those available in the method documentation, where parameters were set as specified in case-specific vignettes. For added provenance tracking, the configuration files include a reference to their sources.

Graph-based SAC methods often use resolution parameters to control cluster granularity that ultimately dictates the number of resultant clusters. To enable fair comparison across metrics requiring fixed cluster counts, we performed binary searches for the resolution values yielding the number of clusters defined in the GT annotation. This approach ensured compatibility with spatially agnostic metrics like adjusted Rand index (ARI) while maintaining method-specific spatial constraints.

Additionally, we included the most prominent single-cell transcriptomics clustering algorithm, Leiden, as implemented in Seurat and Scanpy. See Supplementary Table S1 for a complete overview of the implemented methods.

Metrics

We implemented 17 metrics in the framework, categorized based on their use of GT labels or spatial information. See Supplementary Table S3 for a complete overview of the implemented metrics. In addition to the conventional clustering metrics, we developed two entropy-based metrics. Both metrics require the calculation of Shannon entropy. In our implementation, if we have a vector of cells from different classes (i.e., clusters), the entropy can subsequently be calculated as:

$$H(X) = -\sum_{i=1}^{m} \left(\frac{n_i}{\sum_{j=1}^{m} n_j} \cdot \log \left(\frac{n_i}{\sum_{j=1}^{m} n_j} \right) \right)$$

where m is the number of classes, n_i is the occurrence of class i in vector X, and $n_i / \sum_{j=1}^{m} n_j$ is the empirical probability of class i.

Table 1: An overview of the datasets used in this study. FF = fresh frozen. FFPE = formalin-fixed paraffin-embedded. GT = ground truth.

Name	Species	Tissue	Type	Slices	Date	Citation	Technology	Readout	Panel	Resolution	GT
cosmx_liver	Human	Liver (Normal and HCC)	FFPE	2	2023	Nanostring	CosMx	Imaging	1000	sub-cellular	Computational
cosmx_lung	Human	Lung (NSCLC)	FFPE	5	2022	[75]	CosMx	Imaging	960	sub-cellular	Computational
abc_atlas_wmb_thalamus	Mouse	Brain (thalamus)	FF	59	2023	[4]	MERSCOPE	Imaging	500	sub-cellular	Manual
merfish_devheart	Human	Heart	FF	4	2024	[76]	MERFISH	Imaging	238	sub-cellular	Computational
STARmap_plus	Mouse	Brain	FF	20	2023	[77]	STARmap PLUS	Imaging	1022	sub-cellular	Manual
xenium-ffpe-bc-idc	Human	Breast	FFPE	1	2023	10X Genomics	Xenium	Imaging	380	sub-cellular	Manual
xenium-mouse-brain-SergioSalas	Mouse	Brain (coronal section)	FF	1	2023	10X Genomics	Xenium	Imaging	247	sub-cellular	Manual
slideseq2_olfactory_bulb	Mouse	Brain (olfactory bulb)	FF	20	2022	[80]	Slide-seqV2	Sequencing	N/A	single-cell	Manual
stereoseq_liver	Mouse	Liver	FF	6	2024	[45]	Stereo-seq	Sequencing	N/A	single-cell	Computational
stereoseq_mouse_embryo	Mouse	Embryo	FF	53	2022	[13]	Stereo-seq	Sequencing	N/A	single-cell	Computational
libd_dlpfc	Human	Brain (dorsolateral prefrontal cortex)	FF	12	2021	[35]	Visium	Sequencing	N/A	mini-bulk	Manual
osmfish_Ssp	Mouse	Brain (SSp)	FF	1	2018	[81]	osmFISH	Imaging	33	single-cell	Computational
visium_breast_cancer_SEDR	Human	Breast (invasive ductal carcinoma)	FF	1	2020	[85]	Visium	Sequencing	N/A	mini-bulk	Manual
visium_chicken_heart	Chicken	Heart	FF	11	2021	[82]	Visium	Sequencing	N/A	mini-bulk	Manual
Visium_hd_cancer_colon	Human	Colon (CRC)	FFPE	1	2024	[54]	Visium HD	Sequencing	N/A	mini-bulk / single-cell / sub-cellular	Manual

Smoothness entropy (SE)

SE quantifies the spatial coherence of clustering results by measuring label consistency within local neighborhoods. The SE is calculated by identifying the K-nearest neighbors for each spot or cell in the dataset. Subsequently, the entropy is calculated spot-wise across the labels of the spot and its K neighbors. Spot-wise entropy is then averaged to provide the SE for the sample on a particular label. For SE shown in Figure 3, K is set to 6.

Cross-method entropy (CME)

CME identifies regions of uncertainty by measuring label discordance across multiple clustering results. To generate the CME for a dataset, a set of labelings with the same number of clusters is aligned by finding the optimal matches across different labelings using the Hungarian method implemented in the R package clue (version 0.3_66) [86]. Once the labelings are aligned, spot-wise entropy is calculated across the labelings from different methods. The labeling alignment requires a reference labeling where other labelings are aligning against. To avoid stochasticity from arbitrary selection of reference labeling, the entropy is calculated once for each instance where a labeling is selected as the reference. The final spot-wise CME is calculated by averaging the entropies from different reference labeling cases.

Computational framework

SACCELERATOR is orchestrated by a modular Snakemake [87] workflow, which coordinates all computational steps for standardized and reproducible analysis. The framework is organized into distinct modules for datasets, SAC methods, metrics, and consensus clustering. Each dataset module consisted of a script to download the dataset, GT annotations, images, and other metadata and store them in a standardized format. Likewise, each method and metric module consisted of a separate script, ensuring interoperability with the standardized data structure produced by other modules. Consensus clustering within SACCELERATOR is implemented as a three-step process: results aggregation, base clustering selection, and consensus generation. Each of these steps is documented with a minimally executable example, clear instructions to add new instances, and explanatory notes in its respective folder on the GitHub repository. To guarantee reproducibility and prevent dependency conflicts, each script is linked to a version-pinned conda environment file. A centralized configuration file allows the Snakemake workflow to specify parameters for each module, such as which datasets to download and the number of clusters to identify.

Consensus clustering algorithms

Three consensus clustering approaches were implemented in the framework and applied in the paper: Latent Class Analysis (LCA), K-modes, and weight-based consensus. Both LCA and K-modes [88] approaches were implemented via the R package diceR [89]. The weighted-based consensus incorporates a Bregmannian divergence framework [52, 53] utilizing the weighted Jensen-Shannon Divergence (JSD) as the loss function [90]:

$$\min_{S,\{\omega_m\}} \sum_{m=1}^{M} \omega_m \, \mathrm{JSD}(S \parallel S^{(m)}) + \lambda \sum_{m=1}^{M} \omega_m \log \omega_m$$

subject to

$$\sum_{m=1}^{M} \omega_m = 1, \quad \omega_m \geq 0.$$

where M is the number of base clusterings, S is the binary similarity matrix for consensus results, $S^{(m)}$ is the binary similarity matrix of individual base clusterings, and ω_m are the respective weights of each base clustering. The second term is an entropy regularization of the weights to prevent the inclination of the binary similarity matrix to certain base clusterings. The resulting binary similarity matrix S was clustered using the Leiden algorithm to generate the final consensus clusters.

Base clustering selection

Base clustering selection is an essential process for generating consensus clusterings. As implemented in SACCELERATOR, this process is designed to be flexible and context-dependent, reflecting the expert-in-the-loop workflow. There is no universally optimal criterion for selecting the "best" base clusterings for consensus clustering; rather, selection should be tailored to the specific technological platform and biological context under study. In the analysis-specific sections below, we describe in detail how base clusterings are selected based on different biological settings.

Meta-benchmark analysis

We collated ARI values for the Visium LIBD DLPFC dataset from original method papers and benchmarking studies, sourcing data from the main text and supplementary material of published articles, GitHub repositories, and Zenodo repositories. In total, we gathered results for 22 SAC methods that we implemented and three benchmarking studies [5, 16, 17]. Among these, 17 method papers and one benchmarking study [16] reported ARI values for the DLPFC dataset. BayesSpace, one of the earliest SAC methods, was the most frequently benchmarked, with ARI reported in 16 studies. We excluded studies that only reported summary statistics (e.g., mean or median ARI) or results from a single tissue slice. For comparisons of self-reported ARI with those from other studies, we excluded methods that had not been independently applied by at least one subsequent study.

Computational resource management

All SACCELERATOR computational jobs were orchestrated using Snakemake (v8.14.0) for workflow management and SLURM (v21.08.5) for workload management on the de.NBI cloud infrastructure. Each method was executed using a dedicated allocation of 10 CPU threads and 500 GB of RAM per job. For each sample, the maximum allowed runtime was set to 48 hours. If a job exceeded this limit, it was automatically terminated and recorded as a failure for that sample. Resource utilization, including wall-clock runtime and peak memory usage, was monitored and recorded using Snakemake's built-in benchmarking functionality. Benchmarking data were parsed and summarized using custom Python scripts.

Configuration benchmarking

For the Visium DLPFC dataset, we calculated the ARI values for all methods using the same number of clusters and method-specific configurations. Methods without additional configurations were excluded. This resulted in ARI values for 18 methods, each with 2 to 6 configurations. For details on the configuration settings, refer to the section on Spatially Aware Clustering Methods.

GT granularity analysis

To generate the PCA plots for the LIBD DLPFC dataset shown in Figure 2A and B, we performed quality control on slice 151673 by filtering out spots with less than 600 total mRNA counts or more than 28 percent

mitochondrial transcript content. Spots with fewer than 10 cells detected were also excluded. The 10% most highly variable genes were detected for the sample via `getTopHVGs()` function in R package `scran` (version 1.34.0) [91]. PCA was run on the highly variable genes via function `runPCA()` in the R package `scater` (version 1.34.1) [92]. To identify border spots, we constructed a K-nearest neighbor graph based on the spatial coordinates of the spots using function `kNN()` from R package `dbscan` (version 1.2.0) [93] with $k = 4$. We filtered out neighbors with a distance larger than 1.5. A spot was deemed a border spot if any of its neighbors, including itself, did not belong to the same cluster as the GT labels.

For the Xenium mouse brain dataset and the Visium breast Ccncer dataset, SAC results were generated using the default configurations of five methods (Supplementary Table S2). To examine the relationship between ARI and cluster granularity, all methods were configured to identify various numbers of clusters for the datasets (Xenium: 5,7,9,11; Visium: 3,4,5,6,7). The ARI against the GT annotation was then calculated using the implemented workflow.

For the Stereo-seq mouse liver dataset, we subsetted the datasets to the 925 unique zonation-related genes reported in three studies [47–49]. Five methods were then run on both the full and subsetted liver dataset with a memory and runtime cap of 500 GB and 48 hours. All methods except STAGATE managed to generate clustering results. The four remaining methods were configured to generate between 3 and 9 clusters. In addition to the default 9-layer GT, we aggregated the layers into 3 regions according to the original study. Specifically, Layer 1 and 2 were aggregated as the pericentral cluster, Layer 4 to 6 were merged into a midzonal cluster, and the rest were the periportal cluster. ARI values were calculated for SAC results against both the original nine-layer and the aggregated three-region GTs.

LIBD DLPFC Visium consensus analysis

All base clusterings generated from the workflow for slice 151673 (with 5, 7, or 9 clusters; Supplementary Table S2) were aggregated to compute pairwise ARIs (Figure 3A). To identify a concordant block of SAC methods, we applied cutoffs to the hierarchical clustering tree (euclidean distance, complete linkage) of the pairwise ARIs, which revealed two groupings, one of which represented a highly concordant set of 14 distinct clustering methods (Figure 3A; blue box). From this set of concordant methods, base clusterings were selected as input to LCA consensus clustering [50], separately for each number of clusters (5, 7, 9), according to their smoothness entropy, with priority given to smoother base clusterings. For example, Figure 3D ("7 clusters, 12 methods") represents a consensus clustering of the 12 smoothest (i.e., lowest SE) 7-cluster base clusterings. For the leave-one-out validation, a consensus clustering (LCA) was generated for each method, separately for each number of clusters. Each consensus comprised the 6 smoothest base clusterings of the starting set of methods (blue box of Figure 3A), excluding the method itself.

Thalamus consensus analysis

Thalamus sample C57BL6J-638850_6800 was selected to showcase the consensus workflow. We first generated SAC results of the sample from existing method configurations in the workflow (Supplementary Table S2). Then, we filtered out any base clusterings with a prominent class imbalance, where one cluster comprised more than 90% of the cells. Then, the eight methods with the lowest SE were selected as base clusterings for the consensus clustering for all three consensus algorithms. A consensus was calculated separately for base clusterings with 16, 20, and 24 clusters. The cluster numbers were selected based on expert suggestions.

Visium HD consensus analysis

The dataset was prepared as described in the dataset section above. Multiple configurations were employed for the tested SAC methods (Supplementary Table S2). For the full-section analysis, the pipeline was configured to identify 5, 6, 7, 9, 11, and 14 clusters. For the consensus calling, the sample was subset to only the neoplasm region, and the pipeline was configured to identify six clusters. The base clustering selection was done similarly to the LIBD DLPFC example (see above), via selecting a core set of "concordant" methods according to pairwise ARIs and setting cutoffs on the hierarchical clustering tree (black box in Figure 5E). As with the LIBD DLPFC consensus approach, the consensus clustering was generated using the LCA algorithm [50]. Marker genes for the neoplastic region and dysplasia were calculated with the tie-corrected Wilcoxon rank-sum test implemented in Scanpy [94].

Data and code availability

The SACCELERATOR workflow and all relevant code to run the analysis are available as open-source software on GitHub (https://github.com/SpatialHackathon/SACCELERATOR). All code for reproducing results presented in this study, including figures and collected ARIs for the meta benchmark are available via https://github.com/SpatialHackathon/SpaceHack2023_study. Links to raw data are provided in the Datasets section. All filtered data, intermediate results, and final results are deposited on Zenodo (https://zenodo.org/records/15487520).

Competing interests

RG has received consulting income (payments made to the Lausanne University Hospital) from Takeda, Arcellx, Sanofi, Owkin, and declares ownership in Ozette Technologies.

Funding

This research has received funding from the Federal Ministry of Education and Research of Germany in the framework of SAGE (project number 031L0265) and CNAScope (01KD2443), and the German Research Foundation in the framework of CRC/TR 412 (35081457). This research was supported by an NWO Gravitation project: BRAINSCAPES: A Roadmap from Neurogenetics to Neurobiology (NWO: 024.004.012). MDR acknowledges support from the University Research Priority Program Evolution in Action at the University of Zurich, as well as the Swiss National Science Foundation (project grant 310030_204869). MAT and BL were supported by the National Institute of Neurological Disorders and Stroke of the National Institutes of Health under Award Number U19NS123714. JS and RG were supported by the Swiss National Science Foundation(SNSF) grant 320030_215550. FH was founded by the German Federal Ministry of Research, Technology and Space (BMFTR; 01KD2206A,B,L,M,/SATURN3). The authors thankfully acknowledge the computer resources and the technical support provided by the BMBF-funded de.NBI Cloud within the German Network for Bioinformatics Infrastructure (de.NBI) (031A537B, 031A533A, 031A538A, 031A533B, 031A535A, 031A537C, 031A534A, 031A532B).

Author contributions

NI, AM, MDR conceptualized the project. NMB implemented the concept of the benchmarking framework. NMB, FH, KB, JS, MAT, PK performed data curation. JS, KB, PC, NMB, SHD, MDR, PK performed formal analysis. NI and MDR acquired finances. NMB, JS, MDR, SK, SG, ME, PK, SHD, PC developed and designed the methodology. NMB, FH, JS, KB, PC, SHD, PK implemented and tested the softwares.

RE, ST, RG provided critical resources. ST established the SpaceHack cloud infrastructures. NI, MDR, AM, CK, RE, RG, BL performed supervision. MAT, AEH, MZ performed validation. JS, KB, PK, MDR, PC, MAT performed visualization. NI, AM, SHD, JS, MDR, KB, PC, MAT, PK wrote the original draft of the manuscript, and NI, AM, FH, SHD, JS, MDR, MAT, MR reviewed and edited the manuscript.

Acknowledgments

We thank the organizers and participants of the de.NBI BioHackathon SpaceHack 2.0 project in Bielefeld, Germany in December 2023 (Supplementary Table S4). The SpaceHack 2.0 project was funded by the German Federal Ministry of Education and Research in the frame of de.NBI & ELIXIR-DE (W-de.NBI-001). We also thank Martin Braun and Valentin Schneider-Lunitz for their support with the cloud.

References

[1] Marx, V.: Method of the year: spatially resolved transcriptomics. Nat. Methods **18**(1), 9–14 (2021)

[2] Cheng, M., Jiang, Y., Xu, J., Mentis, A.-F.A., Wang, S., Zheng, H., Sahu, S.K., Liu, L., Xu, X.: Spatially resolved transcriptomics: a comprehensive review of their technological advances, applications, and challenges. J. Genet. Genomics **50**(9), 625–640 (2023)

[3] Schürch, C.M., Bhate, S.S., Barlow, G.L., Phillips, D.J., Noti, L., Zlobec, I., Chu, P., Black, S., Demeter, J., McIlwain, D.R., Kinoshita, S., Samusik, N., Goltsev, Y., Nolan, G.P.: Coordinated cellular neighborhoods orchestrate antitumoral immunity at the colorectal cancer invasive front. Cell **182**(5), 1341–135919 (2020)

[4] Yao, Z., Velthoven, C.T.J., Kunst, M., Zhang, M., McMillen, D., Lee, C., Jung, W., Goldy, J., Abdelhak, A., Aitken, M., Baker, K., Baker, P., Barkan, E., Bertagnolli, D., Bhandiwad, A., Bielstein, C., Bishwakarma, P., Campos, J., Carey, D., Casper, T., Chakka, A.B., Chakrabarty, R., Chavan, S., Chen, M., Clark, M., Close, J., Crichton, K., Daniel, S., DiValentin, P., Dolbeare, T., Ellingwood, L., Fiabane, E., Fliss, T., Gee, J., Gerstenberger, J., Glandon, A., Gloe, J., Gould, J., Gray, J., Guilford, N., Guzman, J., Hirschstein, D., Ho, W., Hooper, M., Huang, M., Hupp, M., Jin, K., Kroll, M., Lathia, K., Leon, A., Li, S., Long, B., Madigan, Z., Malloy, J., Malone, J., Maltzer, Z., Martin, N., McCue, R., McGinty, R., Mei, N., Melchor, J., Meyerdierks, E., Mollenkopf, T., Moonsman, S., Nguyen, T.N., Otto, S., Pham, T., Rimorin, C., Ruiz, A., Sanchez, R., Sawyer, L., Shapovalova, N., Shepard, N., Slaughterbeck, C., Sulc, J., Tieu, M., Torkelson, A., Tung, H., Valera Cuevas, N., Vance, S., Wadhwani, K., Ward, K., Levi, B., Farrell, C., Young, R., Staats, B., Wang, M.-Q.M., Thompson, C.L., Mufti, S., Pagan, C.M., Kruse, L., Dee, N., Sunkin, S.M., Esposito, L., Hawrylycz, M.J., Waters, J., Ng, L., Smith, K., Tasic, B., Zhuang, X., Zeng, H.: A high-resolution transcriptomic and spatial atlas of cell types in the whole mouse brain. Nature **624**(7991), 317–332 (2023)

[5] Yuan, Z., Zhao, F., Lin, S., Zhao, Y., Yao, J., Cui, Y., Zhang, X.-Y., Zhao, Y.: Benchmarking spatial clustering methods with spatially resolved transcriptomics data. Nat. Methods **21**(4), 712–722 (2024)

[6] Shang, L., Zhou, X.: Spatially aware dimension reduction for spatial transcriptomics. Nat. Commun. **13**(1), 7203 (2022)

[7] Jackson, K.C., Booeshaghi, A.S., Gálvez-Merchán, , Moses, L., Chari, T., Kim, A., Pachter, L.: Identification of spatial homogeneous regions in tissues with concordex. bioRxivorg, 2023–0628546949 (2024)

[8] Bhate, S.S., Barlow, G.L., Schürch, C.M., Nolan, G.P.: Tissue schematics map the specialization of immune tissue motifs and their appropriation by tumors. Cell Syst. **13**(2), 109–1306 (2022)

[9] Varrone, M., Tavernari, D., Santamaria-Martínez, A., Walsh, L.A., Ciriello, G.: CellCharter reveals spatial cell niches associated with tissue remodeling and cell plasticity. Nat. Genet. **56**(1), 74–84 (2024)

[10] Schaar, A.C., Tejada-Lapuerta, A., Palla, G., Gutgesell, R., Halle, L., Minaeva, M., Vornholz, L., Dony, L., Drummer, F., Bahrami, M., Theis, F.J.: Nicheformer: a foundation model for single-cell and spatial omics. bioRxiv, 2024–0415589472 (2024)

[11] Scadden, D.T.: Nice neighborhood: emerging concepts of the stem cell niche. Cell **157**(1), 41–50 (2014)

[12] Singhal, V., Chou, N., Lee, J., Yue, Y., Liu, J., Chock, W.K., Lin, L., Chang, Y.-C., Teo, E.M.L., Aow, J., Lee, H.K., Chen, K.H., Prabhakar, S.: BANKSY unifies cell typing and tissue domain segmentation for scalable spatial omics data analysis. Nat. Genet. **56**(3), 431–441 (2024)

[13] Chen, A., Liao, S., Cheng, M., Ma, K., Wu, L., Lai, Y., Qiu, X., Yang, J., Xu, J., Hao, S., Wang, X., Lu, H., Chen, X., Liu, X., Huang, X., Li, Z., Hong, Y., Jiang, Y., Peng, J., Liu, S., Shen, M., Liu, C., Li, Q., Yuan, Y., Wei, X., Zheng, H., Feng, W., Wang, Z., Liu, Y., Wang, Z., Yang, Y., Xiang, H., Han, L., Qin, B., Guo, P., Lai, G., Muñoz-Cánoves, P., Maxwell, P.H., Thiery, J.P., Wu, Q.-F., Zhao, F., Chen, B., Li, M., Dai, X., Wang, S., Kuang, H., Hui, J., Wang, L., Fei, J.-F., Wang, O., Wei, X., Lu, H., Wang, B., Liu, S., Gu, Y., Ni, M., Zhang, W., Mu, F., Yin, Y., Yang, H., Lisby, M., Cornall, R.J., Mulder, J., Uhlén, M., Esteban, M.A., Li, Y., Liu, L., Xu, X., Wang, J.: Spatiotemporal transcriptomic atlas of mouse organogenesis using DNA nanoball-patterned arrays. Cell **185**(10), 1777–179221 (2022)

[14] Bidanta, S., Börner, K., Herr, B.W. II, Nagy, M., Gustilo, K.S., Bajema, R., Maier, L., Molontay, R., Weber, G.: Functional tissue units in the human reference atlas. bioRxiv (2023)

[15] Eickhoff, S.B., Yeo, B.T.T., Genon, S.: Imaging-based parcellations of the human brain. Nat. Rev. Neurosci. **19**(11), 672–686 (2018)

[16] Hu, Y., Xie, M., Li, Y., Rao, M., Shen, W., Luo, C., Qin, H., Baek, J., Zhou, X.M.: Benchmarking clustering, alignment, and integration methods for spatial transcriptomics. Genome Biol. **25**(1), 212 (2024)

[17] Cheng, A., Hu, G., Li, W.V.: Benchmarking cell-type clustering methods for spatially resolved transcriptomics data. Brief. Bioinform. **24**(1), 475 (2023)

[18] Liu, T., Fang, Z.-Y., Zhang, Z., Yu, Y., Li, M., Yin, M.-Z.: A comprehensive overview of graph neural network-based approaches to clustering for spatial transcriptomics. Comput. Struct. Biotechnol. J. **23**, 106–128 (2024)

[19] Alturkistani, H.A., Tashkandi, F.M., Mohammedsaleh, Z.M.: Histological stains: A literature review and case study. Glob. J. Health Sci. **8**(3), 72–79 (2015)

[20] CZI Single-Cell Biology Program, Abdulla, S., Aevermann, B., Assis, P., Badajoz, S., Bell, S.M., Bezzi, E., Cakir, B., Chaffer, J., Chambers, S., Michael Cherry, J., Chi, T., Chien, J., Dorman, L., Garcia-Nieto, P., Gloria, N., Hastie, M., Hegeman, D., Hilton, J., Huang, T., Infeld, A., Istrate, A.-M., Jelic, I., Katsuya, K., Kim, Y.J., Liang, K., Lin, M., Lombardo, M., Marshall, B., Martin, B., McDade, F., Megill, C., Patel, N., Predeus, A., Raymor, B., Robatmili, B., Rogers, D., Rutherford, E., Sadgat, D., Shin, A., Small, C., Smith, T., Sridharan, P., Tarashansky, A., Tavares, N., Thomas, H., Tolopko, A., Urisko, M., Yan, J., Yeretssian, G., Zamanian, J., Mani, A., Cool, J., Carr, A.: CZ CELL×GENE discover: A single-cell data platform for scalable exploration, analysis and modeling of aggregated data. bioRxiv, 2023–1030563174 (2023)

[21] Tabula Sapiens Consortium*, Jones, R.C., Karkanias, J., Krasnow, M.A., Pisco, A.O., Quake, S.R., Salzman, J., Yosef, N., Bulthaup, B., Brown, P., Harper, W., Hemenez, M., Ponnusamy, R., Salehi, A., Sanagavarapu, B.A., Spallino, E., Aaron, K.A., Concepcion, W., Gardner, J.M., Kelly, B., Neidlinger, N.,

Wang, Z., Crasta, S., Kolluru, S., Morri, M., Tan, S.Y., Travaglini, K.J., Xu, C., Alcántara-Hernández, M., Almanzar, N., Antony, J., Beyersdorf, B., Burhan, D., Calcuttawala, K., Carter, M.M., Chan, C.K.F., Chang, C.A., Chang, S., Colville, A., Culver, R.N., Cvijović, I., D'Amato, G., Ezran, C., Galdos, F.X., Gillich, A., Goodyer, W.R., Hang, Y., Hayashi, A., Houshdaran, S., Huang, X., Irwin, J.C., Jang, S., Juanico, J.V., Kershner, A.M., Kim, S., Kiss, B., Kong, W., Kumar, M.E., Kuo, A.H., Li, B., Loeb, G.B., Lu, W.-J., Mantri, S., Markovic, M., McAlpine, P.L., Morree, A., Mrouj, K., Mukherjee, S., Muser, T., Neuhöfer, P., Nguyen, T.D., Perez, K., Puluca, N., Qi, Z., Rao, P., Raquer-McKay, H., Schaum, N., Scott, B., Seddighzadeh, B., Segal, J., Sen, S., Sikandar, S., Spencer, S.P., Steffes, L.C., Subramaniam, V.R., Swarup, A., Swift, M., Van Treuren, W., Trimm, E., Veizades, S., Vijayakumar, S., Vo, K.C., Vorperian, S.K., Wang, W., Weinstein, H.N.W., Winkler, J., Wu, T.T.H., Xie, J., Yung, A.R., Zhang, Y., Detweiler, A.M., Mekonen, H., Neff, N.F., Sit, R.V., Tan, M., Yan, J., Bean, G.R., Charu, V., Forgó, E., Martin, B.A., Ozawa, M.G., Silva, O., Toland, A., Vemuri, V.N.P., Afik, S., Awayan, K., Botvinnik, O.B., Byrne, A., Chen, M., Dehghannasiri, R., Gayoso, A., Granados, A.A., Li, Q., Mahmoudabadi, G., McGeever, A., Olivieri, J.E., Park, M., Ravikumar, N., Stanley, G., Tan, W., Tarashansky, A.J., Vanheusden, R., Wang, P., Wang, S., Xing, G., Dethlefsen, L., Ezran, C., Gillich, A., Hang, Y., Ho, P.-Y., Irwin, J.C., Jang, S., Leylek, R., Liu, S., Maltzman, J.S., Metzger, R.J., Phansalkar, R., Sasagawa, K., Sinha, R., Song, H., Swarup, A., Trimm, E., Veizades, S., Wang, B., Beachy, P.A., Clarke, M.F., Giudice, L.C., Huang, F.W., Huang, K.C., Idoyaga, J., Kim, S.K., Kuo, C.S., Nguyen, P., Rando, T.A., Red-Horse, K., Reiter, J., Relman, D.A., Sonnenburg, J.L., Wu, A., Wu, S.M., Wyss-Coray, T.: The tabula sapiens: A multiple-organ, single-cell transcriptomic atlas of humans. Science **376**(6594), 4896 (2022)

[22] Xu, C., Prete, M., Webb, S., Jardine, L., Stewart, B.J., Hoo, R., He, P., Meyer, K.B., Teichmann, S.A.: Automatic cell-type harmonization and integration across human cell atlas datasets. Cell **186**(26), 5876–589120 (2023)

[23] Domínguez Conde, C., Xu, C., Jarvis, L.B., Rainbow, D.B., Wells, S.B., Gomes, T., Howlett, S.K., Suchanek, O., Polanski, K., King, H.W., Mamanova, L., Huang, N., Szabo, P.A., Richardson, L., Bolt, L., Fasouli, E.S., Mahbubani, K.T., Prete, M., Tuck, L., Richoz, N., Tuong, Z.K., Campos, L., Mousa, H.S., Needham, E.J., Pritchard, S., Li, T., Elmentaite, R., Park, J., Rahmani, E., Chen, D., Menon, D.K., Bayraktar, O.A., James, L.K., Meyer, K.B., Yosef, N., Clatworthy, M.R., Sims, P.A., Farber, D.L., Saeb-Parsy, K., Jones, J.L., Teichmann, S.A.: Cross-tissue immune cell analysis reveals tissue-specific features in humans. Science **376**(6594), 5197 (2022)

[24] Wibberg, D.: SpaceHack 2.0. de.NBI. Accessed: 2025-4-30

[25] Zhao, E., Stone, M.R., Ren, X., Guenthoer, J., Smythe, K.S., Pulliam, T., Williams, S.R., Uytingco, C.R., Taylor, S.E.B., Nghiem, P., Bielas, J.H., Gottardo, R.: Spatial transcriptomics at subspot resolution with BayesSpace. Nat. Biotechnol. **39**(11), 1375–1384 (2021)

[26] Long, Y., Ang, K.S., Li, M., Chong, K.L.K., Sethi, R., Zhong, C., Xu, H., Ong, Z., Sachaphibulkij, K., Chen, A., Zeng, L., Fu, H., Wu, M., Lim, L.H.K., Liu, L., Chen, J.: Spatially informed clustering, integration, and deconvolution of spatial transcriptomics with GraphST. Nat. Commun. **14**(1), 1155 (2023)

[27] Xu, C., Jin, X., Wei, S., Wang, P., Luo, M., Xu, Z., Yang, W., Cai, Y., Xiao, L., Lin, X., Liu, H., Cheng, R., Pang, F., Chen, R., Su, X., Hu, Y., Wang, G., Jiang, Q.: DeepST: identifying spatial domains in

spatial transcriptomics by deep learning. Nucleic Acids Res. **50**(22), 131 (2022)

[28] Zong, Y., Yu, T., Wang, X., Wang, Y., Hu, Z., Li, Y.: conST: an interpretable multi-modal contrastive learning framework for spatial transcriptomics. bioRxiv, 2022–0114476408 (2022)

[29] Hu, J., Li, X., Coleman, K., Schroeder, A., Ma, N., Irwin, D.J., Lee, E.B., Shinohara, R.T., Li, M.: SpaGCN: Integrating gene expression, spatial location and histology to identify spatial domains and spatially variable genes by graph convolutional network. Nat. Methods **18**(11), 1342–1351 (2021)

[30] Chidester, B., Zhou, T., Alam, S., Ma, J.: SPICEMIX enables integrative single-cell spatial modeling of cell identity. Nat. Genet. **55**(1), 78–88 (2023)

[31] Dong, K., Zhang, S.: Deciphering spatial domains from spatially resolved transcriptomics with an adaptive graph attention auto-encoder. Nat. Commun. **13**(1), 1739 (2022)

[32] Li, Z., Zhou, X.: BASS: multi-scale and multi-sample analysis enables accurate cell type clustering and spatial domain detection in spatial transcriptomic studies. Genome Biol. **23**(1), 168 (2022)

[33] Zhu, J., Yang, Y.: scMEB: a fast and clustering-independent method for detecting differentially expressed genes in single-cell RNA-seq data. BMC Genomics **24**(1), 280 (2023)

[34] Liu, W., Liao, X., Yang, Y., Lin, H., Yeong, J., Zhou, X., Shi, X., Liu, J.: Joint dimension reduction and clustering analysis of single-cell RNA-seq and spatial transcriptomics data. Nucleic Acids Res. **50**(12), 72 (2022)

[35] Maynard, K.R., Collado-Torres, L., Weber, L.M., Uytingco, C., Barry, B.K., Williams, S.R., Catallini, J.L. 2nd, Tran, M.N., Besich, Z., Tippani, M., Chew, J., Yin, Y., Kleinman, J.E., Hyde, T.M., Rao, N., Hicks, S.C., Martinowich, K., Jaffe, A.E.: Transcriptome-scale spatial gene expression in the human dorsolateral prefrontal cortex. Nat. Neurosci. **24**(3), 425–436 (2021)

[36] Mölder, F., Jablonski, K.P., Letcher, B., Hall, M.B., Tomkins-Tinch, C.H., Sochat, V., Forster, J., Lee, S., Twardziok, S.O., Kanitz, A., Wilm, A., Holtgrewe, M., Rahmann, S., Nahnsen, S., Köster, J.: Sustainable data analysis with snakemake. F1000Res. **10**, 33 (2021)

[37] Luo, S., Germain, P.-L., Meyenn, F., Robinson, M.D.: On metrics for subpopulation detection in single-cell and spatial omics data. bioRxiv, 2024–1128625845 (2024)

[38] Guo, L., Hu, Z., Zhao, C., Xu, X., Wang, S., Xu, J., Dong, J., Cai, Z.: Data filtering and its prioritization in pipelines for spatial segmentation of mass spectrometry imaging. Anal. Chem. **93**(11), 4788–4793 (2021)

[39] Ståhl, P.L., Salmén, F., Vickovic, S., Lundmark, A., Navarro, J.F., Magnusson, J., Giacomello, S., Asp, M., Westholm, J.O., Huss, M., Mollbrink, A., Linnarsson, S., Codeluppi, S., Borg, , Pontén, F., Costea, P.I., Sahlén, P., Mulder, J., Bergmann, O., Lundeberg, J., Frisén, J.: Visualization and analysis of gene expression in tissue sections by spatial transcriptomics. Science **353**(6294), 78–82 (2016)

[40] Nagendran, M., Sapida, J., Arthur, J., Yin, Y., Tuncer, S.D., Anaparthy, N., Gupta, A., Serra, M., Patterson, D., Tentori, A.: 1457 visium HD enables spatially resolved, single-cell scale resolution mapping of FFPE human breast cancer tissue. In: Regular and Young Investigator Award Abstracts, vol. 11. BMJ

Publishing Group Ltd, ??? (2023)

[41] Stickels, R.R., Murray, E., Kumar, P., Li, J., Marshall, J.L., Di Bella, D.J., Arlotta, P., Macosko, E.Z., Chen, F.: Highly sensitive spatial transcriptomics at near-cellular resolution with slide-seqV2. Nat. Biotechnol. **39**(3), 313–319 (2021)

[42] Zeng, H., Huang, J., Zhou, H., Meilandt, W.J., Dejanovic, B., Zhou, Y., Bohlen, C.J., Lee, S.-H., Ren, J., Liu, A., Tang, Z., Sheng, H., Liu, J., Sheng, M., Wang, X.: Integrative in situ mapping of single-cell transcriptional states and tissue histopathology in a mouse model of alzheimer's disease. Nat. Neurosci. **26**(3), 430–446 (2023)

[43] Wang, G., Moffitt, J.R., Zhuang, X.: Multiplexed imaging of high-density libraries of RNAs with MERFISH and expansion microscopy. Sci. Rep. **8**(1), 4847 (2018)

[44] You, Y., Fu, Y., Li, L., Zhang, Z., Jia, S., Lu, S., Ren, W., Liu, Y., Xu, Y., Liu, X., Jiang, F., Peng, G., Sampath Kumar, A., Ritchie, M.E., Liu, X., Tian, L.: Systematic comparison of sequencing-based spatial transcriptomic methods. Nat. Methods **21**(9), 1743–1754 (2024)

[45] Xu, J., Guo, P., Hao, S., Shangguan, S., Shi, Q., Volpe, G., Huang, K., Zuo, J., An, J., Yuan, Y., Cheng, M., Deng, Q., Zhang, X., Lai, G., Nan, H., Wu, B., Shentu, X., Wu, L., Wei, X., Jiang, Y., Huang, X., Pan, F., Song, Y., Li, R., Wang, Z., Liu, C., Liu, S., Li, Y., Yang, T., Xu, Z., Du, W., Li, L., Ahmed, T., You, K., Dai, Z., Li, L., Qin, B., Li, Y., Lai, L., Qin, D., Chen, J., Fan, R., Li, Y., Hou, J., Ott, M., Sharma, A.D., Cantz, T., Schambach, A., Kristiansen, K., Hutchins, A.P., Göttgens, B., Maxwell, P.H., Hui, L., Xu, X., Liu, L., Chen, A., Lai, Y., Esteban, M.A.: A spatiotemporal atlas of mouse liver homeostasis and regeneration. Nat. Genet. **56**(5), 953–969 (2024)

[46] Jungermann, K., Kietzmann, T.: Zonation of parenchymal and nonparenchymal metabolism in liver. Annu. Rev. Nutr. **16**(1), 179–203 (1996)

[47] Halpern, K.B., Shenhav, R., Matcovitch-Natan, O., Toth, B., Lemze, D., Golan, M., Massasa, E.E., Baydatch, S., Landen, S., Moor, A.E., Brandis, A., Giladi, A., Avihail, A.S., David, E., Amit, I., Itzkovitz, S.: Single-cell spatial reconstruction reveals global division of labour in the mammalian liver. Nature **542**(7641), 352–356 (2017)

[48] Hildebrandt, F., Andersson, A., Saarenpää, S., Larsson, L., Van Hul, N., Kanatani, S., Masek, J., Ellis, E., Barragan, A., Mollbrink, A., Andersson, E.R., Lundeberg, J., Ankarklev, J.: Spatial transcriptomics to define transcriptional patterns of zonation and structural components in the mouse liver. Nat. Commun. **12**(1), 7046 (2021)

[49] Dobie, R., Wilson-Kanamori, J.R., Henderson, B.E.P., Smith, J.R., Matchett, K.P., Portman, J.R., Wallenborg, K., Picelli, S., Zagorska, A., Pendem, S.V., Hudson, T.E., Wu, M.M., Budas, G.R., Breckenridge, D.G., Harrison, E.M., Mole, D.J., Wigmore, S.J., Ramachandran, P., Ponting, C.P., Teichmann, S.A., Marioni, J.C., Henderson, N.C.: Single-cell transcriptomics uncovers zonation of function in the mesenchyme during liver fibrosis. Cell Rep. **29**(7), 1832–18478 (2019)

[50] Gao, C.X., Wang, S., Zhu, Y., Ziou, M., Teo, S.M., Smith, C.L., Chiu, D., Talhouk, A., Cotton, S.M., Dwyer, D.: Ensemble clustering: A practical tutorial. PsyArXiv (2024)

[51] Luo, H., Kong, F., Li, Y.: Combining multiple clusterings via k-modes algorithm. In: Lecture Notes in Computer Science. Lecture notes in computer science, pp. 308–315. Springer, ??? (2006)

[52] Li, J., Xie, L., Xie, Y., Wang, F.: Bregmannian consensus clustering for cancer subtypes analysis. Comput. Methods Programs Biomed. **189**(105337), 105337 (2020)

[53] Li, H.-S., Tan, Y.-T., Zhang, X.-F.: Enhancing spatial domain detection in spatial transcriptomics with EnSDD. Commun. Biol. **7**(1), 1358 (2024)

[54] Oliveira, M.F., Romero, J.P., Chung, M., Williams, S., Gottscho, A.D., Gupta, A., Pilipauskas, S.E., Mohabbat, S., Raman, N., Sukovich, D., Patterson, D., Taylor, S.E.B., Visium HD Development Team: Characterization of immune cell populations in the tumor microenvironment of colorectal cancer using high definition spatial profiling. bioRxiv, 2024–0604597233 (2024)

[55] O'Reilly, C., Iavarone, E., Yi, J., Hill, S.L.: Rodent somatosensory thalamocortical circuitry: Neurons, synapses, and connectivity. Neurosci. Biobehav. Rev. **126**, 213–235 (2021)

[56] Wang, Q., Ding, S.-L., Li, Y., Royall, J., Feng, D., Lesnar, P., Graddis, N., Naeemi, M., Facer, B., Ho, A., Dolbeare, T., Blanchard, B., Dee, N., Wakeman, W., Hirokawa, K.E., Szafer, A., Sunkin, S.M., Oh, S.W., Bernard, A., Phillips, J.W., Hawrylycz, M., Koch, C., Zeng, H., Harris, J.A., Ng, L.: The allen mouse brain common coordinate framework: A 3D reference atlas. Cell **181**(4), 936–95320 (2020)

[57] Li, Y., Lopez-Huerta, V.G., Adiconis, X., Levandowski, K., Choi, S., Simmons, S.K., Arias-Garcia, M.A., Guo, B., Yao, A.Y., Blosser, T.R., Wimmer, R.D., Aida, T., Atamian, A., Naik, T., Sun, X., Bi, D., Malhotra, D., Hession, C.C., Shema, R., Gomes, M., Li, T., Hwang, E., Krol, A., Kowalczyk, M., Peça, J., Pan, G., Halassa, M.M., Levin, J.Z., Fu, Z., Feng, G.: Distinct subnetworks of the thalamic reticular nucleus. Nature **583**(7818), 819–824 (2020)

[58] Zhu, M., Peng, J., Wang, M., Lin, S., Zhang, H., Zhou, Y., Dai, X., Zhao, H., Yu, Y.-Q., Shen, L., Li, X.-M., Chen, J.: Transcriptomic and spatial GABAergic neuron subtypes in zona incerta mediate distinct innate behaviors. Nat. Commun. **16**(1), 3107 (2025)

[59] Rubio-Teves, M., Martín-Correa, P., Alonso-Martínez, C., Casas-Torremocha, D., García-Amado, M., Timonidis, N., Sheiban, F.J., Bakker, R., Tiesinga, P., Porrero, C., Clascá, F.: Beyond barrels: Diverse thalamocortical projection motifs in the mouse ventral posterior complex. J. Neurosci. **44**(43), 1096242024 (2024)

[60] Maier-Hein, L., Reinke, A., Godau, P., Tizabi, M.D., Buettner, F., Christodoulou, E., Glocker, B., Isensee, F., Kleesiek, J., Kozubek, M., Reyes, M., Riegler, M.A., Wiesenfarth, M., Kavur, A.E., Sudre, C.H., Baumgartner, M., Eisenmann, M., Heckmann-Nötzel, D., Rädsch, T., Acion, L., Antonelli, M., Arbel, T., Bakas, S., Benis, A., Blaschko, M.B., Cardoso, M.J., Cheplygina, V., Cimini, B.A., Collins, G.S., Farahani, K., Ferrer, L., Galdran, A., Ginneken, B., Haase, R., Hashimoto, D.A., Hoffman, M.M., Huisman, M., Jannin, P., Kahn, C.E., Kainmueller, D., Kainz, B., Karargyris, A., Karthikesalingam, A., Kofler, F., Kopp-Schneider, A., Kreshuk, A., Kurc, T., Landman, B.A., Litjens, G., Madani, A., Maier-Hein, K., Martel, A.L., Mattson, P., Meijering, E., Menze, B., Moons, K.G.M., Müller, H., Nichyporuk, B., Nickel, F., Petersen, J., Rajpoot, N., Rieke, N., Saez-Rodriguez, J., Sánchez, C.I., Shetty, S., Smeden, M., Summers, R.M., Taha, A.A., Tiulpin, A., Tsaftaris, S.A., Van Calster, B., Varoquaux, G., Jäger,

P.F.: Metrics reloaded: recommendations for image analysis validation. Nat. Methods **21**(2), 195–212 (2024)

[61] Giroux, V., Rustgi, A.K.: Metaplasia: tissue injury adaptation and a precursor to the dysplasia-cancer sequence. Nat. Rev. Cancer **17**(10), 594–604 (2017)

[62] Fleming, M., Ravula, S., Tatishchev, S.F., Wang, H.L.: Colorectal carcinoma: Pathologic aspects. J. Gastrointest. Oncol. **3**(3), 153–173 (2012)

[63] Guinney, J., Dienstmann, R., Wang, X., Reyniès, A., Schlicker, A., Soneson, C., Marisa, L., Roepman, P., Nyamundanda, G., Angelino, P., Bot, B.M., Morris, J.S., Simon, I.M., Gerster, S., Fessler, E., De Sousa E Melo, F., Missiaglia, E., Ramay, H., Barras, D., Homicsko, K., Maru, D., Manyam, G.C., Broom, B., Boige, V., Perez-Villamil, B., Laderas, T., Salazar, R., Gray, J.W., Hanahan, D., Tabernero, J., Bernards, R., Friend, S.H., Laurent-Puig, P., Medema, J.P., Sadanandam, A., Wessels, L., Delorenzi, M., Kopetz, S., Vermeulen, L., Tejpar, S.: The consensus molecular subtypes of colorectal cancer. Nature medicine **21**(11) (2015)

[64] Niv, Y., Rokkas, T.: Mucin expression in colorectal cancer (CRC): Systematic review and meta-analysis. J. Clin. Gastroenterol. **53**(6), 434–440 (2019)

[65] Morgan, R.G., Mortensson, E., Williams, A.C.: Targeting LGR5 in colorectal cancer: therapeutic gold or too plastic? Br. J. Cancer **118**(11), 1410–1418 (2018)

[66] Prakash, J., Shaked, Y.: The interplay between extracellular matrix remodeling and cancer therapeutics. Cancer Discov. **14**(8), 1375–1388 (2024)

[67] Massagué, J.: TGFbeta in cancer. Cell **134**(2), 215–230 (2008)

[68] Romagnani, P., Lasagni, L., Annunziato, F., Serio, M., Romagnani, S.: CXC chemokines: the regulatory link between inflammation and angiogenesis. Trends Immunol. **25**(4), 201–209 (2004)

[69] Feng, M., Feng, J., Chen, W., Wang, W., Wu, X., Zhang, J., Xu, F., Lai, M.: Lipocalin2 suppresses metastasis of colorectal cancer by attenuating NF-b-dependent activation of snail and epithelial mesenchymal transition. Mol. Cancer **15**(1), 77 (2016)

[70] Flynn, J.M., Melov, S.: SOD2 in mitochondrial dysfunction and neurodegeneration. Free Radic. Biol. Med. **62**, 4–12 (2013)

[71] Durand, M., Kolpak, A., Farrell, T., Elliott, N.A., Shao, W., Brown, M., Volkert, M.R.: The OXR domain defines a conserved family of eukaryotic oxidation resistance proteins. BMC Cell Biol. **8**(1), 13 (2007)

[72] Aghaeepour, N., Finak, G., FlowCAP Consortium, DREAM Consortium, Hoos, H., Mosmann, T.R., Brinkman, R., Gottardo, R., Scheuermann, R.H.: Critical assessment of automated flow cytometry data analysis techniques. Nat. Methods **10**(3), 228–238 (2013)

[73] Hu, C., Wei, N., Yang, J., Wu, H.-J., Zheng, X.: STCC enhances spatial domain detection through consensus clustering of spatial transcriptomics data. Genome Res. (2025)

[74] AssunÇão, R.M., Neves, M.C., Câmara, G., Da Costa Freitas, C.: Efficient regionalization techniques

for socio-economic geographical units using minimum spanning trees. Geogr. Inf. Syst. **20**(7), 797–811 (2006)

[75] He, S., Bhatt, R., Brown, C., Brown, E.A., Buhr, D.L., Chantranuvatana, K., Danaher, P., Dunaway, D., Garrison, R.G., Geiss, G., Gregory, M.T., Hoang, M.L., Khafizov, R., Killingbeck, E.E., Kim, D., Kim, T.K., Kim, Y., Klock, A., Korukonda, M., Kutchma, A., Lewis, Z.R., Liang, Y., Nelson, J.S., Ong, G.T., Perillo, E.P., Phan, J.C., Phan-Everson, T., Piazza, E., Rane, T., Reitz, Z., Rhodes, M., Rosenbloom, A., Ross, D., Sato, H., Wardhani, A.W., Williams-Wietzikoski, C.A., Wu, L., Beechem, J.M.: High-plex imaging of RNA and proteins at subcellular resolution in fixed tissue by spatial molecular imaging. Nat. Biotechnol. **40**(12), 1794–1806 (2022)

[76] Farah, E.N., Hu, R.K., Kern, C., Zhang, Q., Lu, T.-Y., Ma, Q., Tran, S., Zhang, B., Carlin, D., Monell, A., Blair, A.P., Wang, Z., Eschbach, J., Li, B., Destici, E., Ren, B., Evans, S.M., Chen, S., Zhu, Q., Chi, N.C.: Spatially organized cellular communities form the developing human heart. Nature **627**(8005), 854–864 (2024)

[77] Shi, H., He, Y., Zhou, Y., Huang, J., Maher, K., Wang, B., Tang, Z., Luo, S., Tan, P., Wu, M., Lin, Z., Ren, J., Thapa, Y., Tang, X., Chan, K.Y., Deverman, B.E., Shen, H., Liu, A., Liu, J., Wang, X.: Spatial atlas of the mouse central nervous system at molecular resolution. Nature **622**(7983), 552–561 (2023)

[78] Bhuva, D.D., Tan, C.W., Salim, A., Marceaux, C., Pickering, M.A., Chen, J., Kharbanda, M., Jin, X., Liu, N., Feher, K., Putri, G., Tilley, W.D., Hickey, T.E., Asselin-Labat, M.-L., Phipson, B., Davis, M.J.: Library size confounds biology in spatial transcriptomics data. Genome Biol. **25**(1), 99 (2024)

[79] Marco Salas, S., Kuemmerle, L.B., Mattsson-Langseth, C., Tismeyer, S., Avenel, C., Hu, T., Rehman, H., Grillo, M., Czarnewski, P., Helgadottir, S., Tiklova, K., Andersson, A., Rafati, N., Chatzinikolaou, M., Theis, F.J., Luecken, M.D., Wählby, C., Ishaque, N., Nilsson, M.: Optimizing xenium in situ data utility by quality assessment and best-practice analysis workflows. Nat. Methods **22**(4), 813–823 (2025)

[80] Wang, I.-H., Murray, E., Andrews, G., Jiang, H.-C., Park, S.J., Donnard, E., Durán-Laforet, V., Bear, D.M., Faust, T.E., Garber, M., Baer, C.E., Schafer, D.P., Weng, Z., Chen, F., Macosko, E.Z., Greer, P.L.: Spatial transcriptomic reconstruction of the mouse olfactory glomerular map suggests principles of odor processing. Nat. Neurosci. **25**(4), 484–492 (2022)

[81] Codeluppi, S., Borm, L.E., Zeisel, A., La Manno, G., Lunteren, J.A., Svensson, C.I., Linnarsson, S.: Spatial organization of the somatosensory cortex revealed by osmFISH. Nat. Methods **15**(11), 932–935 (2018)

[82] Mantri, M., Scuderi, G.J., Abedini-Nassab, R., Wang, M.F.Z., McKellar, D., Shi, H., Grodner, B., Butcher, J.T., De Vlaminck, I.: Spatiotemporal single-cell RNA sequencing of developing chicken hearts identifies interplay between cellular differentiation and morphogenesis. Nat. Commun. **12**(1), 1771 (2021)

[83] Marconato, L., Palla, G., Yamauchi, K.A., Virshup, I., Heidari, E., Treis, T., Vierdag, W.-M., Toth, M., Stockhaus, S., Shrestha, R.B., Rombaut, B., Pollaris, L., Lehner, L., Vöhringer, H., Kats, I., Saeys, Y., Saka, S.K., Huber, W., Gerstung, M., Moore, J., Theis, F.J., Stegle, O.: SpatialData: an open and universal data framework for spatial omics. Nat. Methods **22**(1), 58–62 (2025)

[84] Chiu, C.-L., Clack, N., the napari community: Napari: A python multi-dimensional image viewer platform

for the research community. Microsc. Microanal. **28**(S1), 1576–1577 (2022)

[85] Xu, H., Fu, H., Long, Y., Ang, K.S., Sethi, R., Chong, K., Li, M., Uddamvathanak, R., Lee, H.K., Ling, J., Chen, A., Shao, L., Liu, L., Chen, J.: Unsupervised spatially embedded deep representation of spatial transcriptomics. Genome Med. **16**(1), 12 (2024)

[86] Hornik, K.: A CLUE for CLUster ensembles. J. Stat. Softw. **14**(12), 1–25 (2005)

[87] Köster, J., Rahmann, S.: Snakemake–a scalable bioinformatics workflow engine. Bioinformatics **28**(19), 2520–2522 (2012)

[88] Huang, J.: A fast clustering algorithm to cluster very large categorical data sets in data mining. DMKD, 0 (1997)

[89] Chiu, D.S., Talhouk, A.: diceR: an R package for class discovery using an ensemble driven approach. BMC Bioinformatics **19**(1), 11 (2018)

[90] Baker, D.N., Dyjack, N., Braverman, V., Hicks, S.C., Langmead, B.: Fast and memory-efficient scRNA-seq k-means clustering with various distances. ACM BCB **2021**, 24 (2021)

[91] Lun, A.T.L., McCarthy, D.J., Marioni, J.C.: A step-by-step workflow for low-level analysis of single-cell RNA-seq data with bioconductor. F1000Res. **5**(2122), 2122 (2016)

[92] McCarthy, D.J., Campbell, K.R., Lun, A.T.L., Wills, Q.F.: Scater: pre-processing, quality control, normalization and visualization of single-cell RNA-seq data in R. Bioinformatics **33**(8), 1179–1186 (2017)

[93] Hahsler, M., Piekenbrock, M., Doran, D.: dbscan: Fast density-based clustering with R. J. Stat. Softw. **91**(1), 1–30 (2019)

[94] Wolf, F.A., Angerer, P., Theis, F.J.: SCANPY: large-scale single-cell gene expression data analysis. Genome Biol. **19**(1), 15 (2018)

Supplementary Materials

Supplementary Figures

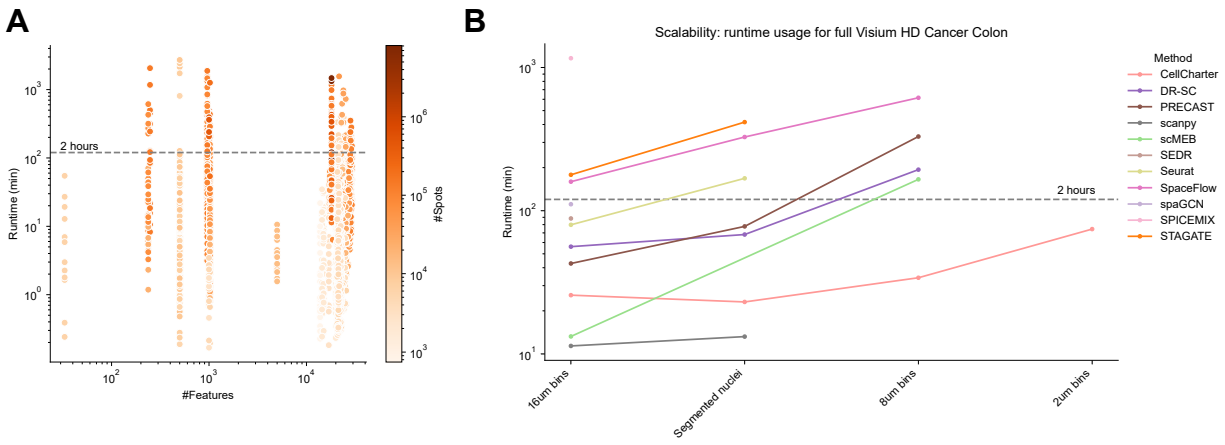

Figure S1: **A**. CPU runtime vs the number of features, colored by the number of spots/cells in the dataset. **B**. CPU runtime of methods on the full Visium HD colorectal cancer dataset across various bin sizes.

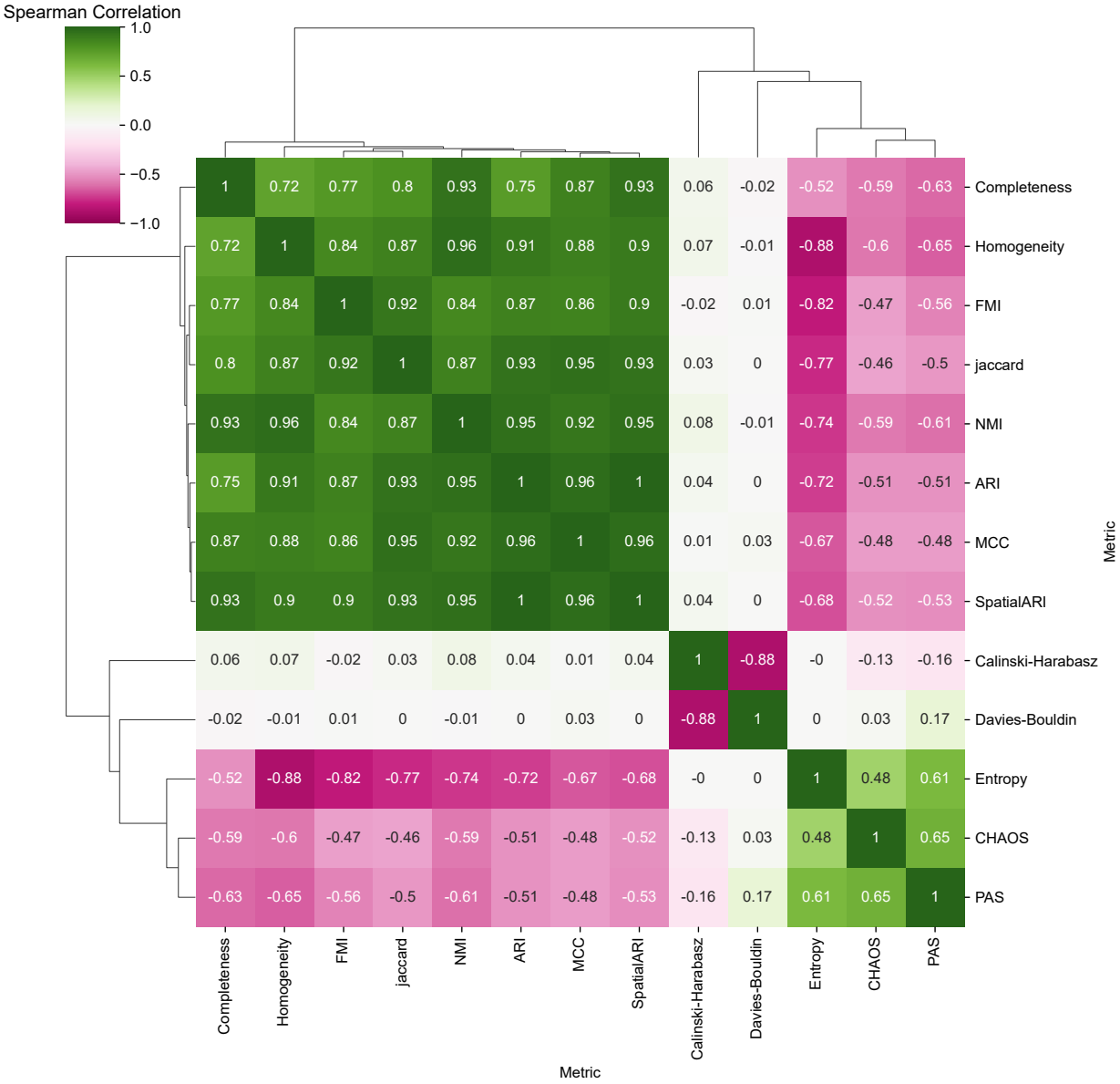

Figure S2: Correlation matrix of different metrics across all methods and samples from the LIBD Visium dataset.

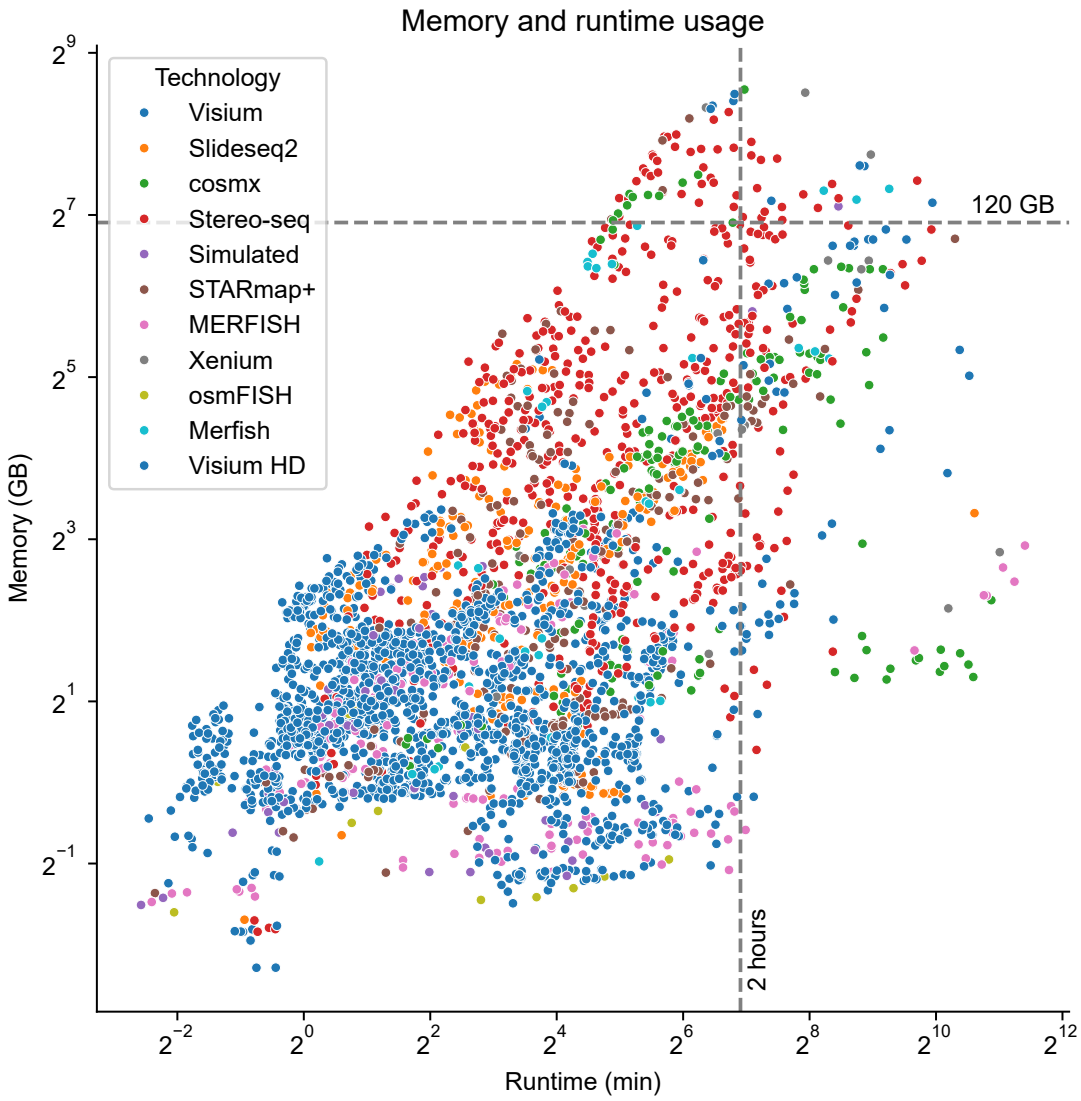

Figure S3: Memory usage vs CPU runtime, colored by the technology of the dataset.

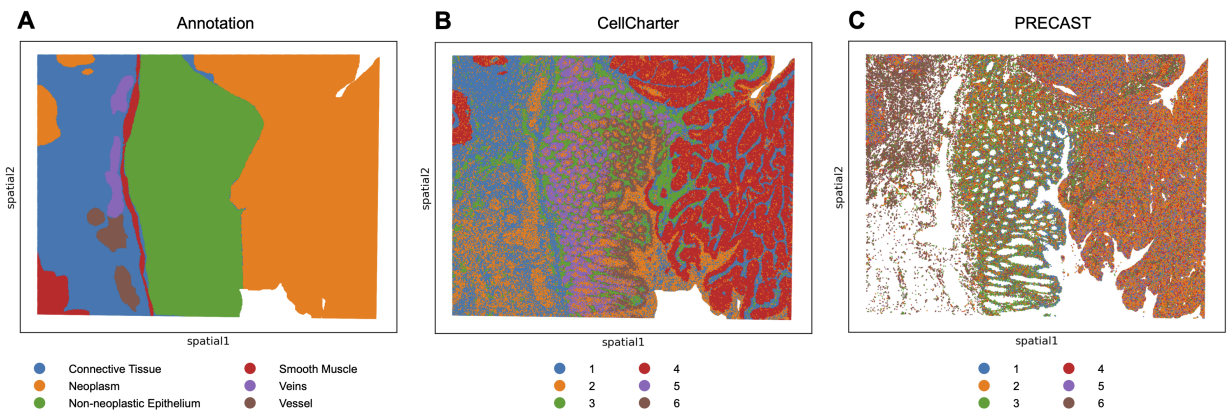

Figure S4: Spatial plots of the cropped Visium HD colon cancer dataset with 2 m bins, colored by **A**. ground truth, **B**. CellCharter clusters, and **C**. PRECAST clusters.

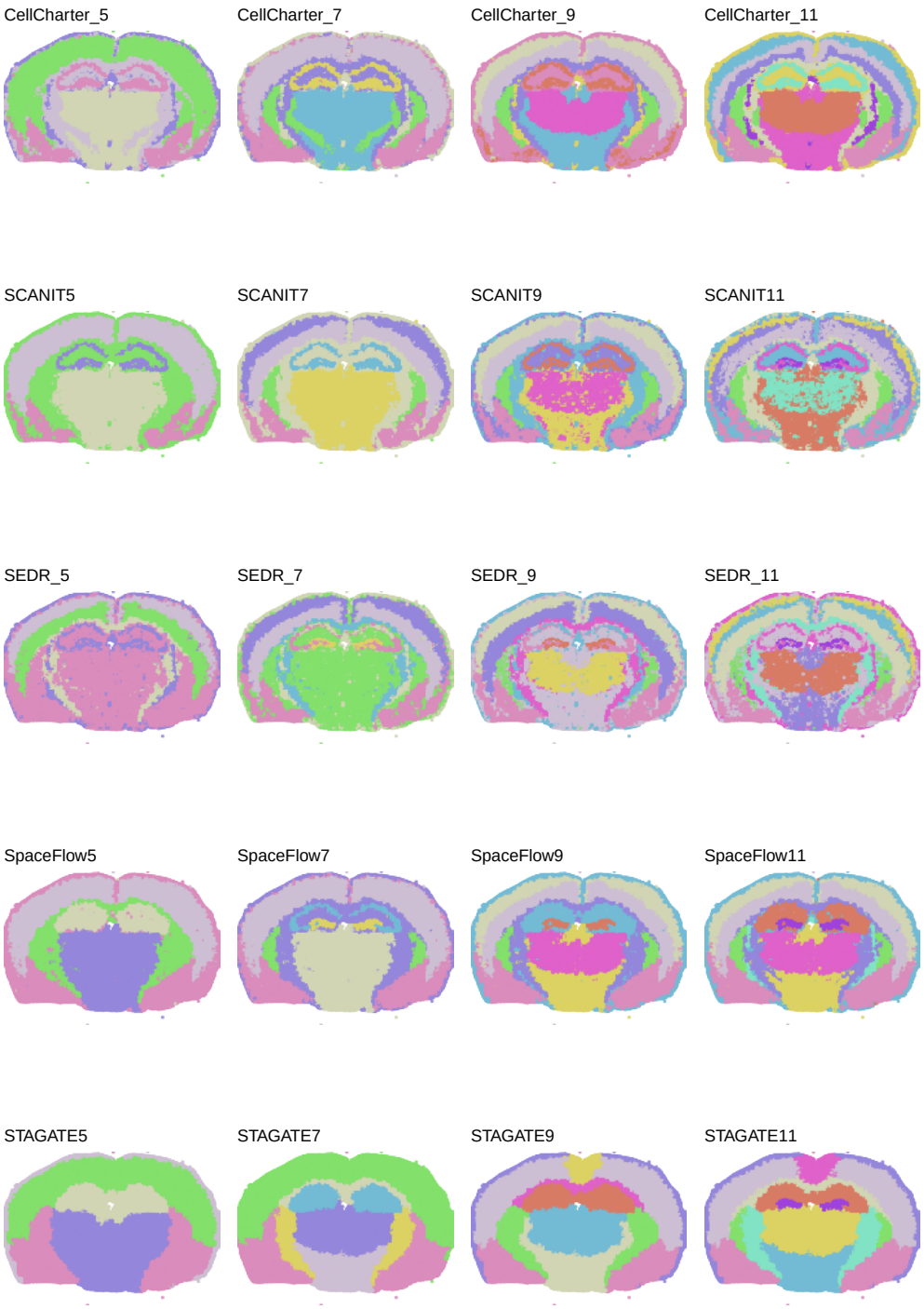

Figure S5: Spatial plots of Xenium mouse brain dataset cluster sweep results.

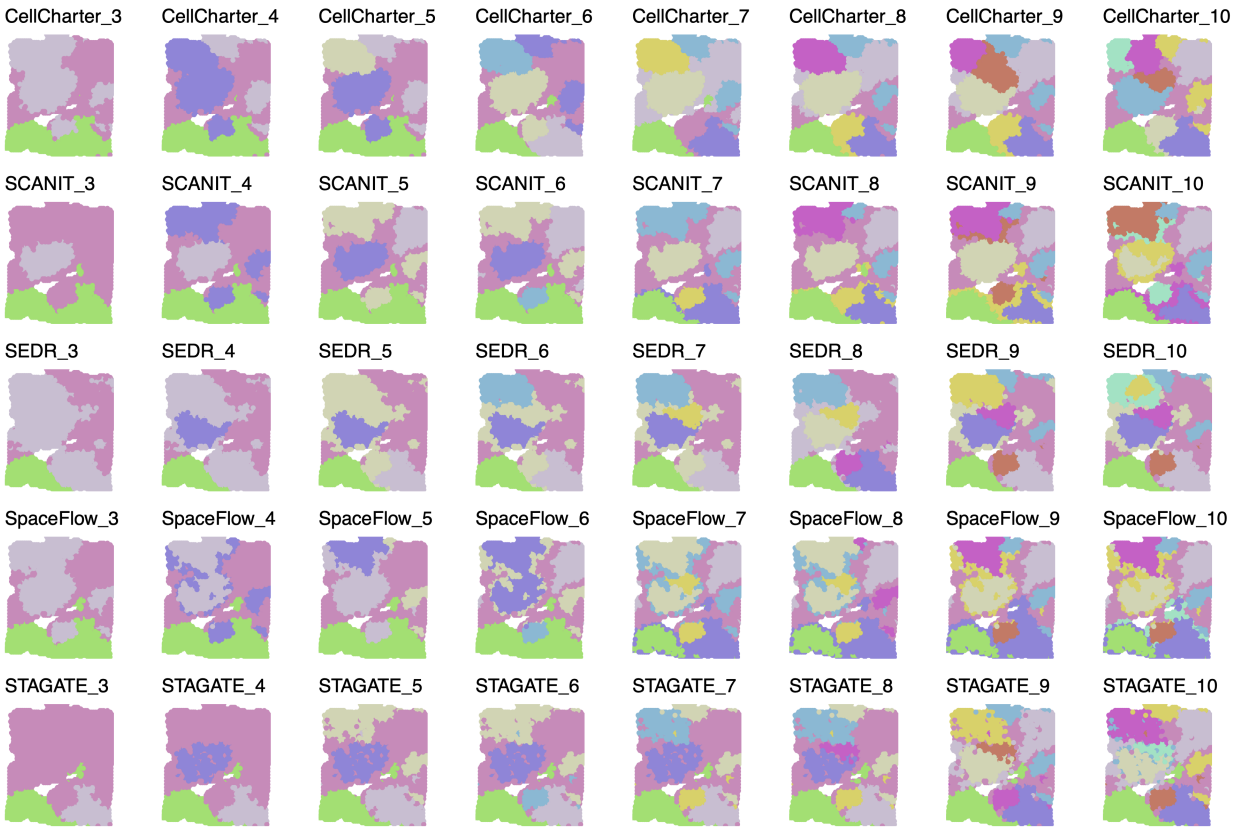

Figure S6: Spatial plots of Visium breast cancer dataset cluster sweep results.

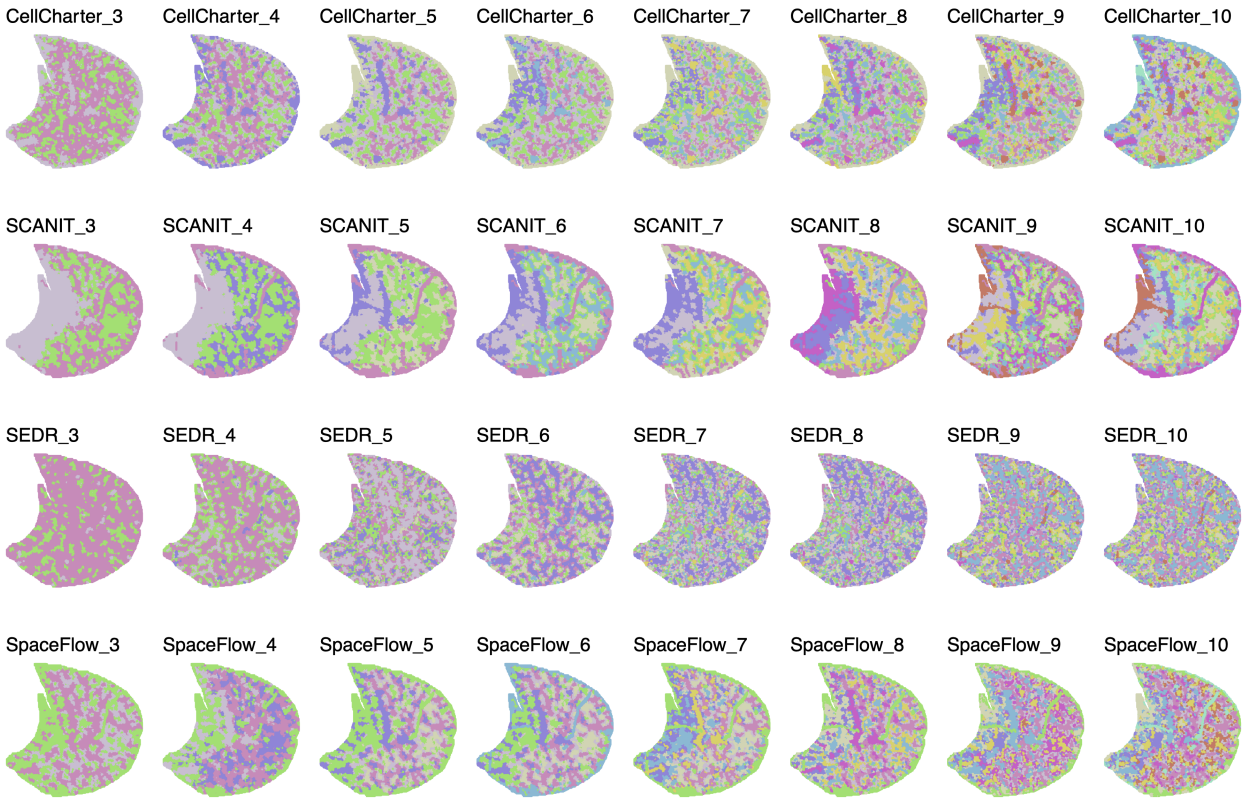

Figure S7: Spatial plots of Stereo-seq mouse liver dataset cluster sweep results with all genes.

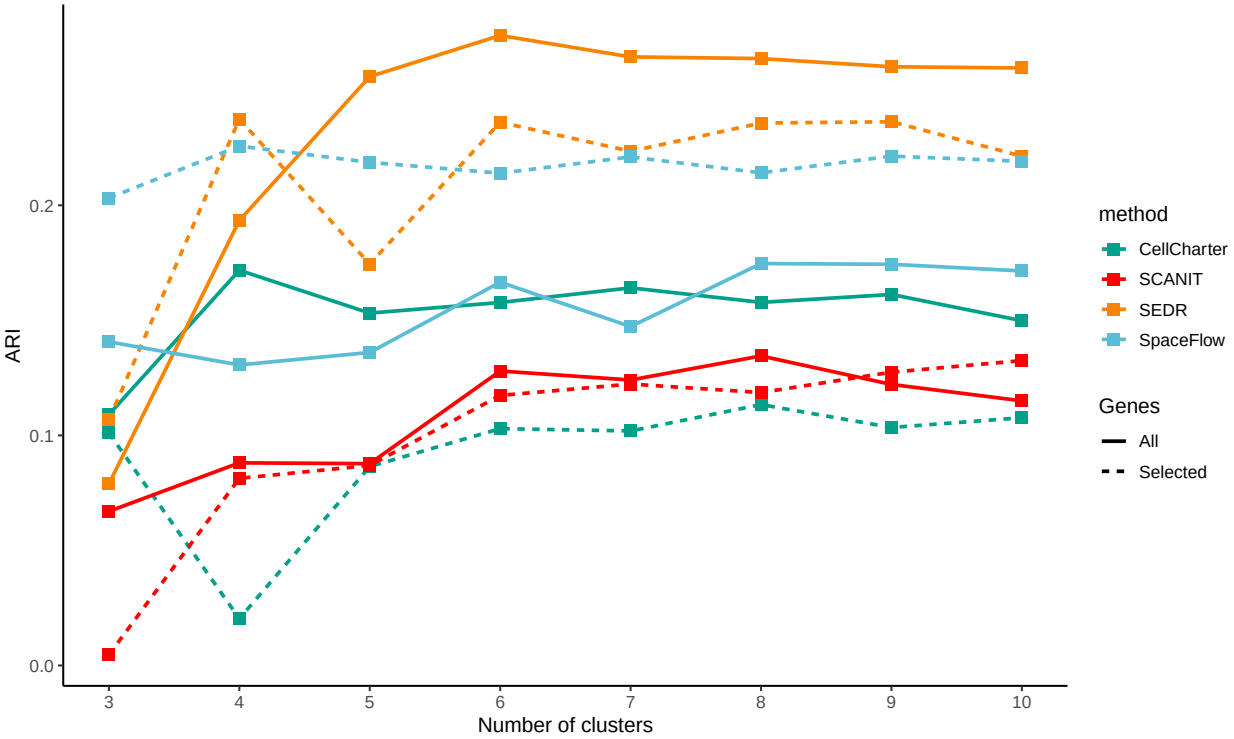

Figure S8: ARI results of Stereo-seq mouse liver datasets with all genes or selected marker genes.

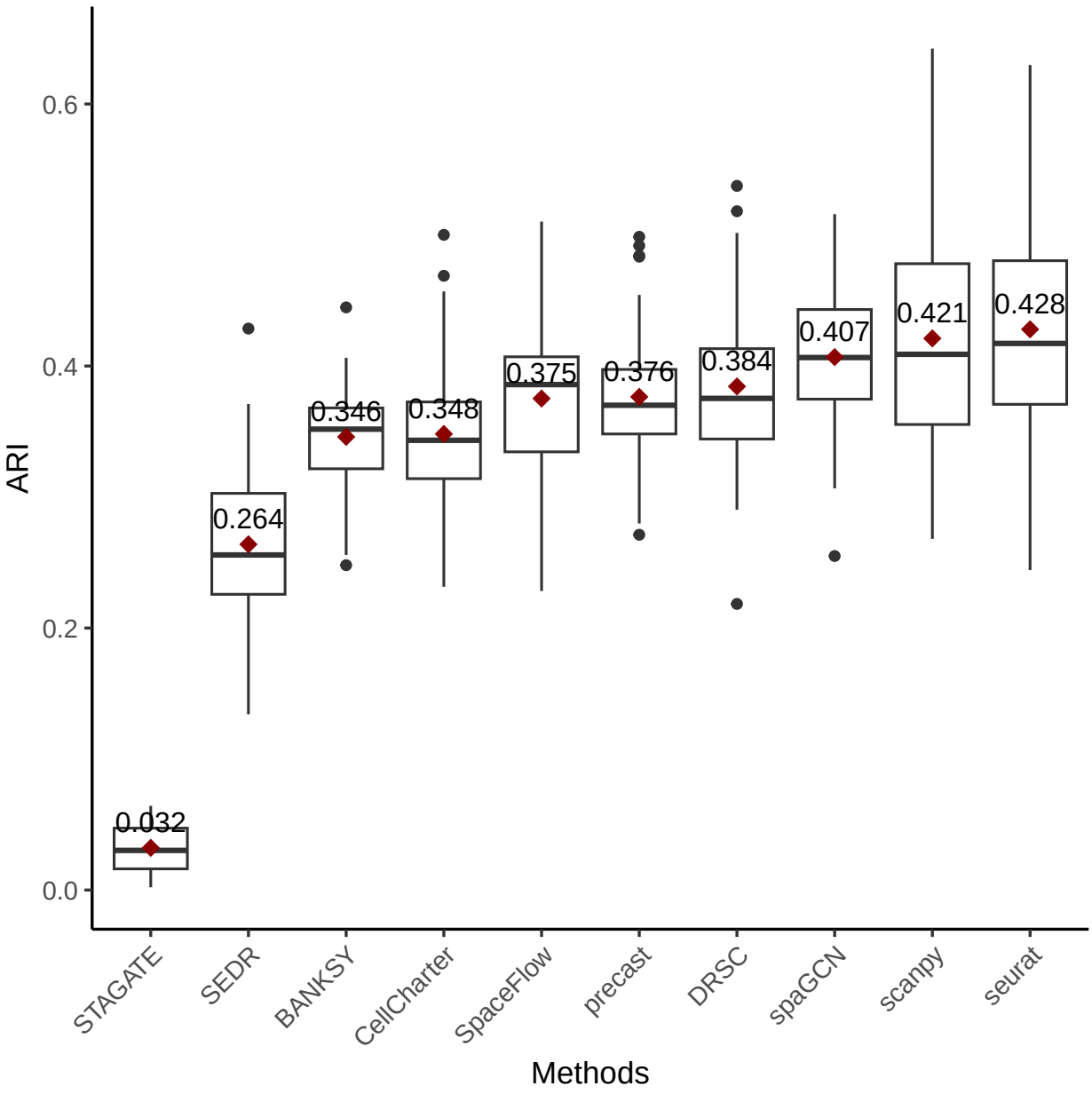

Figure S9: ARI results for Stereo-seq mouse embryo dataset, with mean value indicated in red square.

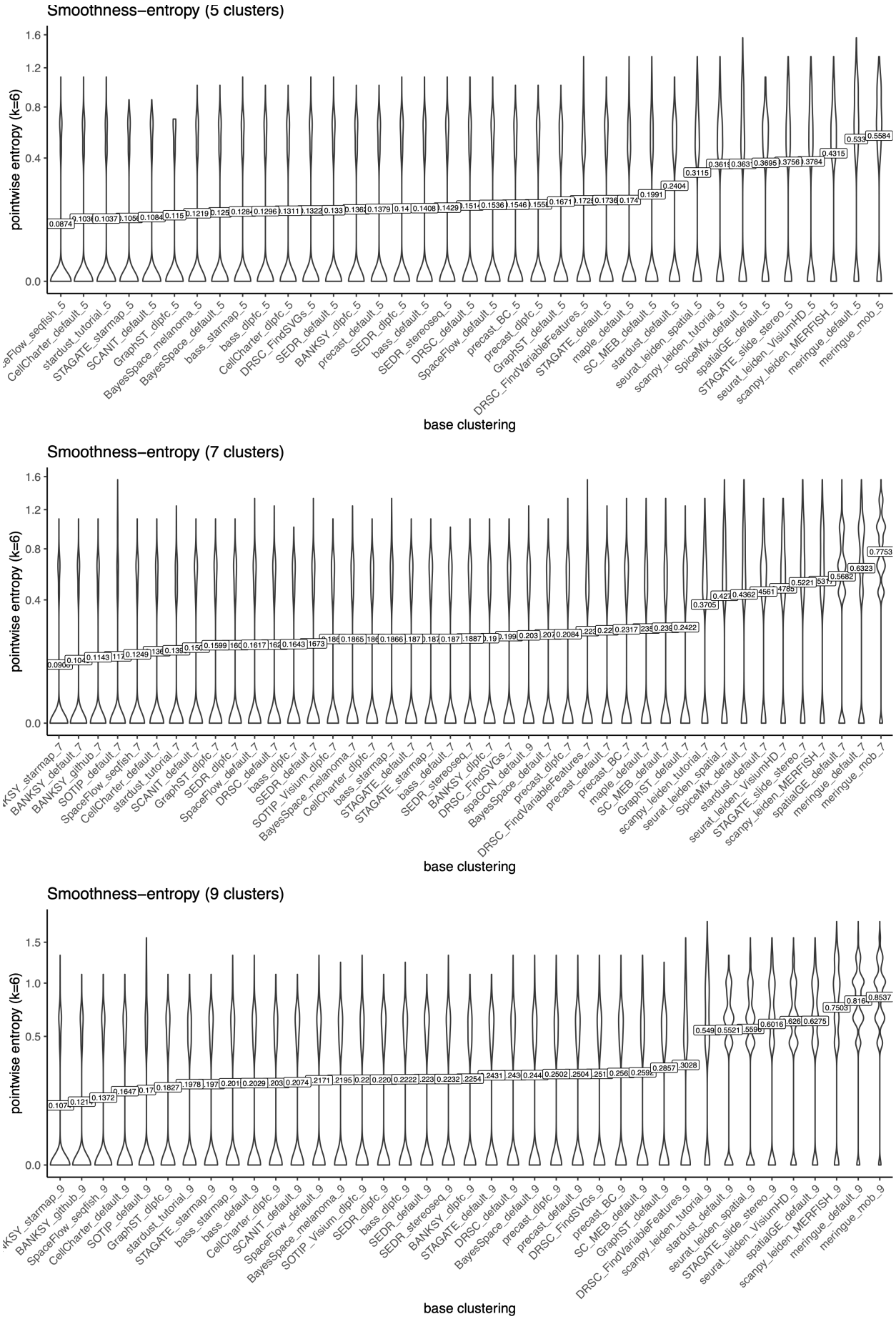

Figure S10: Distributions of smoothness entropy scores for all base clusterings of LIBD DLPFC slice 151673.

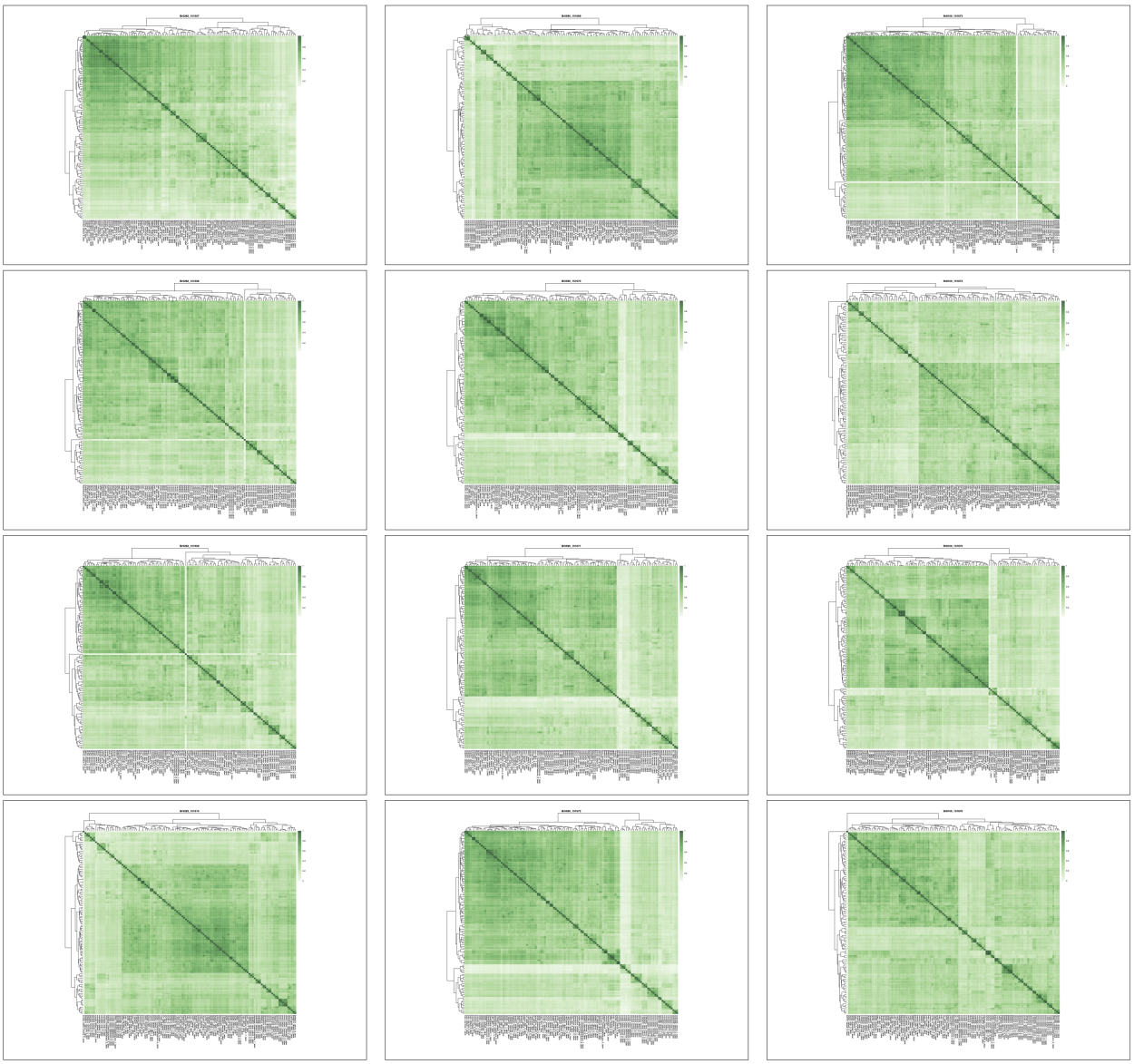

Figure S11: Heatmaps of pairwise ARIs between all base clusterings for each LIBD DLPFC slice. In all cases, we observed a block of concordant methods.

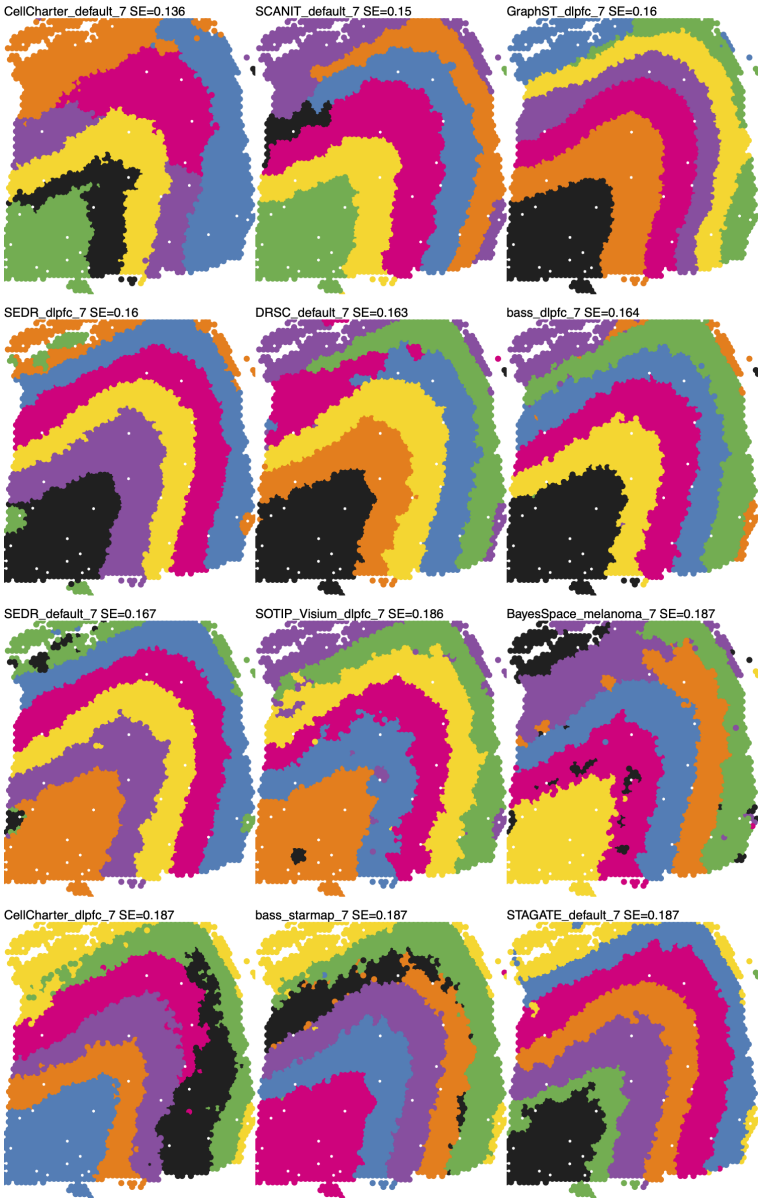

Figure S12: 12 selected base clusterings at 7 clusters to form consensus used for Figure 3B ("consensus_lca") (and represented in Figure 3D) for LIBD DLPFC slice 151673.

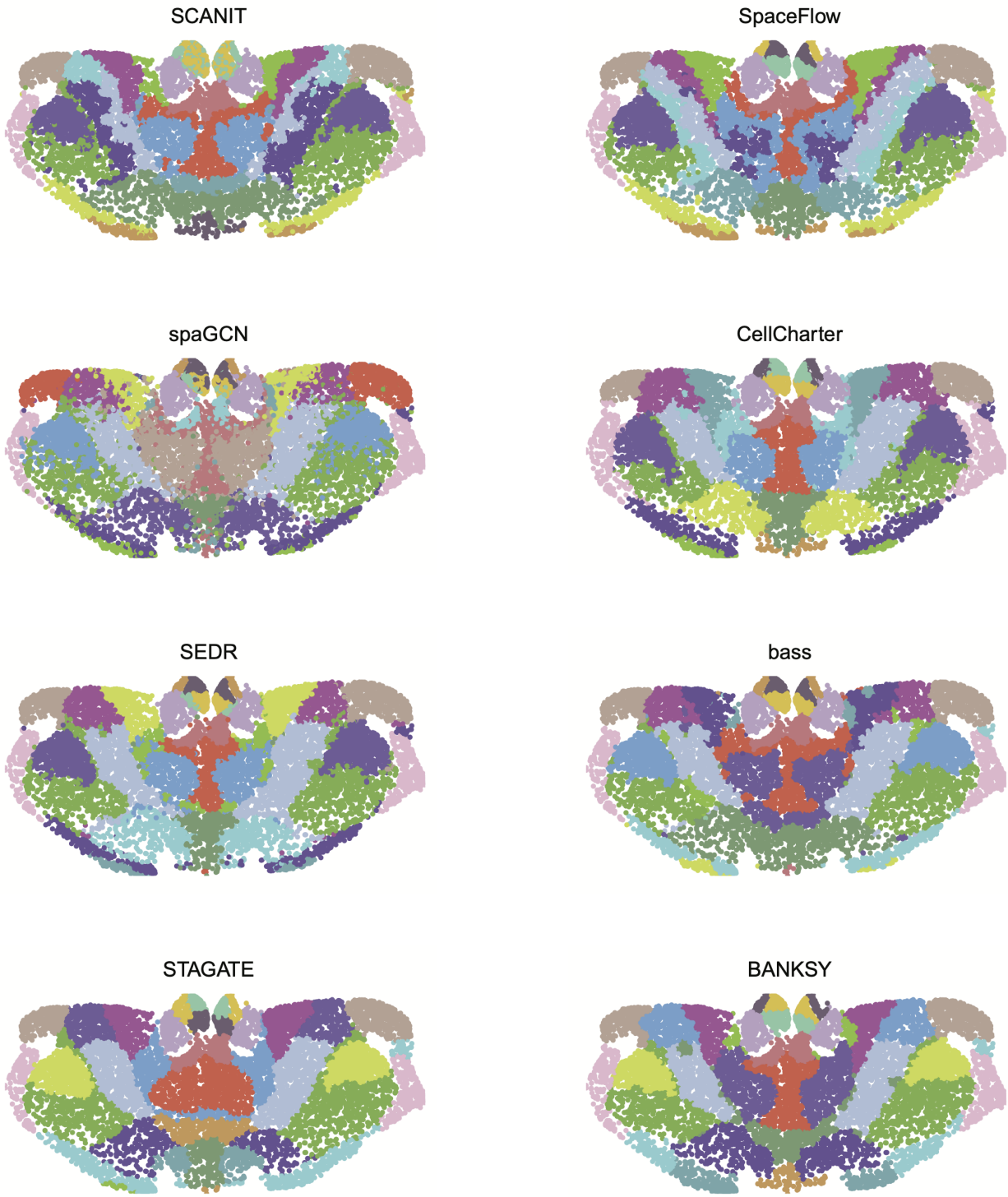

Figure S13: Clusters in the mouse thalamus generated from running 8 SAC methods with the cluster parameter set to 20.

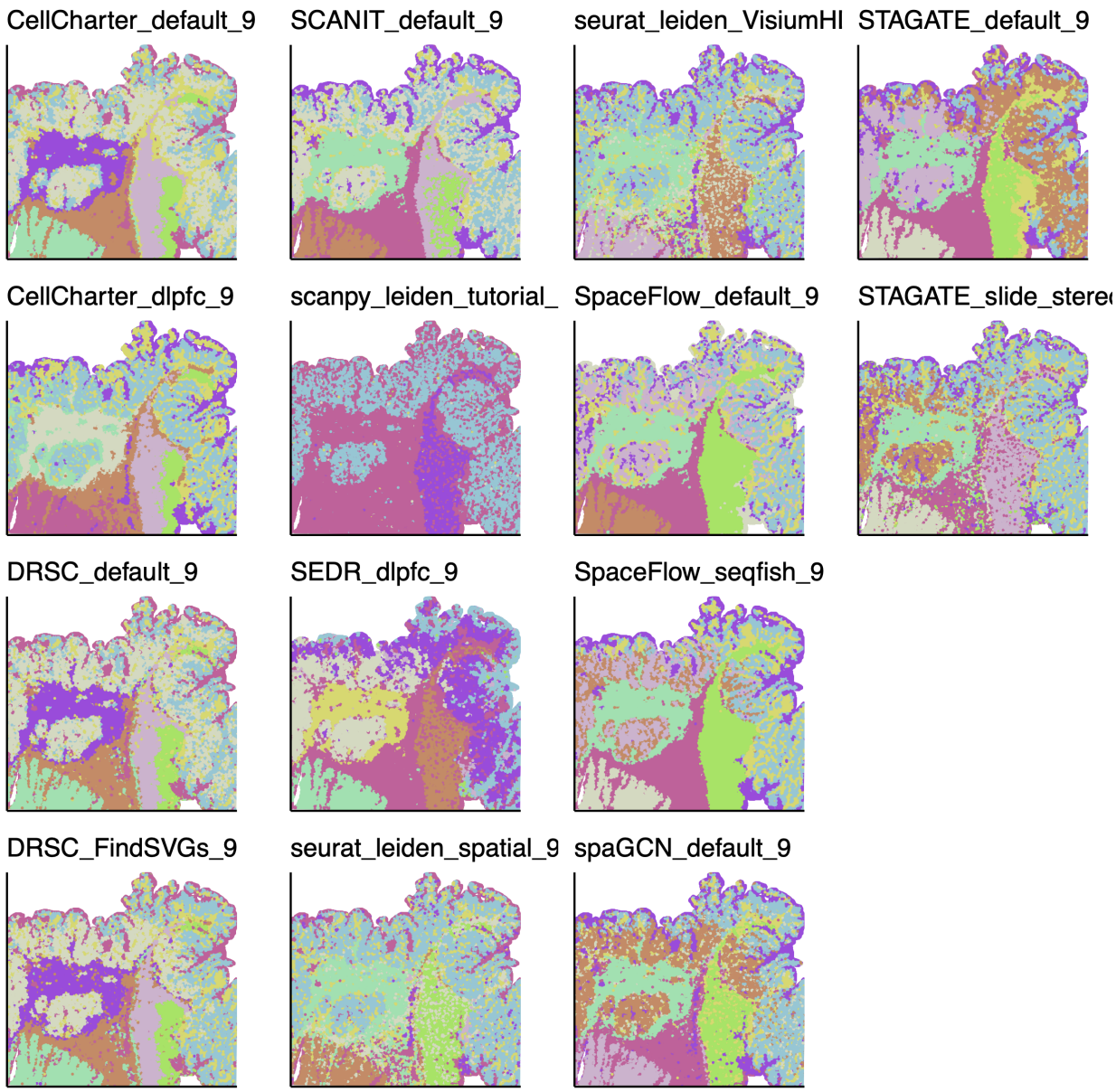

Figure S14: Base clusterings of full Visium HD cancer datasets with 9 clusters for pathologist evaluation.

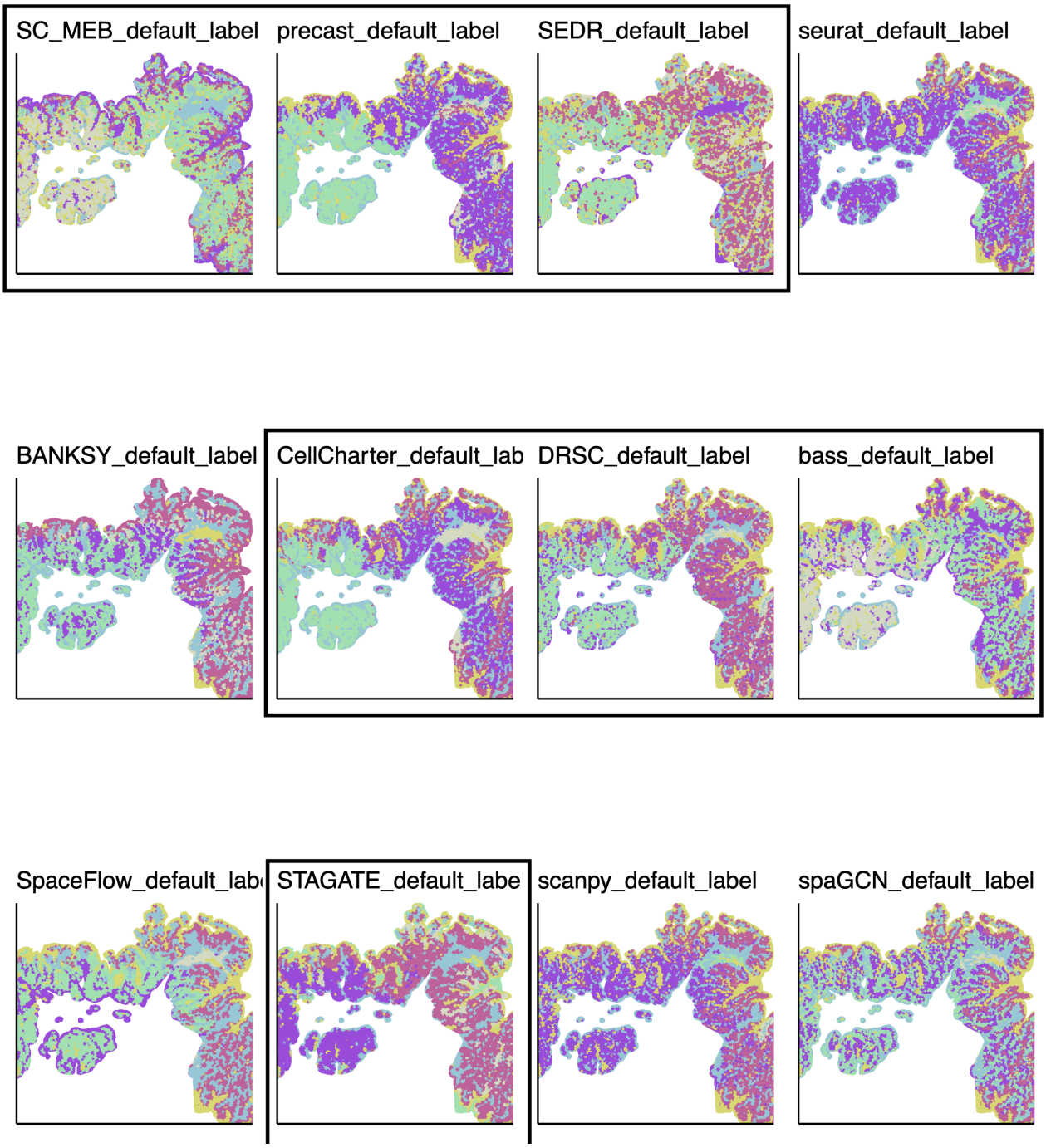

Figure S15: Base clusterings generated for subsetted Visium HD dataset, the instances selected for consensus are enclosed with black boxs.

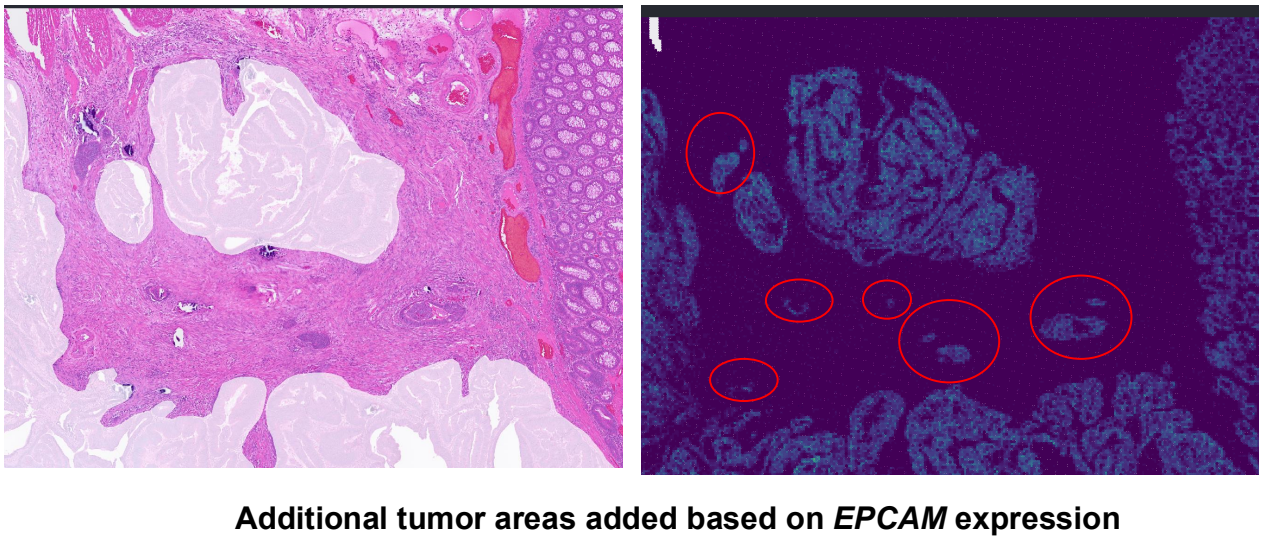

Figure S16: *EPCAM* expression used for fine annotation of the neoplasm. Circles in red were initially missed based solely on the HE

Supplementary Tables

Table S1: Overview of methods. A GitHub commit is only included for methods installed from GitHub without releases.

Name	Version (commit)	Year	Language	Citation
MAPLE	0.99.1 (b173e89)	2024	R	Jeon et al. (2024)
BANKSY	0.99.7 (dbda6fd)	2023	R (+ Python)	Singhal et al. (2023)
PRECAST	1.6.3	2023	R	Liu et al. (2023)
GraphST	1.1.1	2023	Python	Long et al. (2023)
SPICEMIX	0.0.71	2023	Python	Chidester et al. (2023)
CellCharter	0.2.0	2023	Python	Varrone et al. (2023)
STAGATE	1.0.1 (48ce7f8)	2022	Python	Dong & Zhang (2022)
scMEB	1.1	2022	R	Yang et al. (2022)
SpaceFlow	1.0.4	2022	Python	Ren et al. (2022)
DR-SC	3.3	2022	R	Liu et al. (2022)
SCAN-IT	0.1 (ebf3894)	2022	Python	Cang et al. (2022)
SOTIP	1.0 (d3b762c)	2022	Python	Yuan et al. (2022)
Stardust	2.0 (f1b5417)	2022	R	Avesani et al. (2022)
BASS	1.1.0.016 (37980c9)	2022	R	Li & Zhou (2022)
spatialGE	1.2.0.0000	2022	R	Ospina et al. (2022)
SpaGCN	1.2.7	2021	Python	Hu et al. (2021)
BayesSpace	1.10.1	2021	R	Zhao et al. (2021)
SEDR	1.0.0 (8c273af)	2021	Python	Fu et al. (2021)
MERINGUE	1.0 (ca9e2cc)	2021	R	Miller et al. (2021)
Giotto	4.0.0	2021	R (+ Python)	Dries et al. (2021)
Scanpy	1.10.0	2018	Python	Wolf et al. (2018)
Seurat	5.0.1	2018	R	Butler et al. (2018)

Table S2: Overview of method configurations.

Table S3: Overview of metrics.

Name	Requires GT labels	Uses spatial information	Language	Citation
Adjusted Rand Index (ARI)	yes	no	Python	Hubert & Arabie (1985)
Spatial chaos score (CHAOS)	no	yes	R	Shang & Zhou (2022)
Calinski-Harabasz	yes	no	Python	Calinski & Harabasz (2007)
Completeness	yes	no	Python	Rosenberg & Hirschberg (2007)
Davies-Bouldin	no	no	Python	Davies & Bouldin (1979)
Entropy	yes	no	Python	Shannon (1948)
Fowlkes-Mallows Index (FMI)	yes	no	Python	Fowlkes & Mallows (1983)
Homogeneity	yes	no	Python	Rosenberg & Hirschberg (2007)
Local Inverse Simpson's Index (LISI)	yes	no	R	Korsunsky et al. (2019)
Mathew's Correlation Coefficient (MCC)	yes	no	Python	Chicco & Jurman (2020)
Normalized Mutual Information (NMI)	yes	no	R	Strehl & Ghosh (2002)
Percentage of Abnormal Spots (PAS)	no	yes	R	Shang & Zhou (2022)
SpatialARI	yes	yes	R	Luo & Germain (2025)
V measure	yes	no	Python	Rosenberg & Hirschberg (2007)
Cluster specific silhouette	no	no	R	Rousseeuw (1987)
Domain specific F1	yes	no	R	Rijsbergen (1979)
Jaccard	yes	no	Python	Jaccard (1912)

Table S4: SpaceHack 2.0 participants.